Remote Sensing of Environment 169 (2015) 50–74

Contents lists available at ScienceDirect

Remote Sensing of Environment

journal homepage: www.elsevier.com/locate/rse

Improved wet path delays for all ESA and reference altimetric missions

M. Joana Fernandes [a,b,*], Clara Lázaro [a,b], Michaël Ablain [c], Nelson Pires [a,b]

[a] Univ. Porto, Faculdade de Ciências, Porto, Portugal
[b] Centro Interdisciplinar de Investigação Marinha e Ambiental (CIIMAR-CIMAR), Porto, Portugal
[c] Collecte Localisation Satellites, Toulouse, France

ARTICLE INFO

Article history:
Received 27 January 2015
Received in revised form 23 May 2015
Accepted 17 July 2015
Available online 13 August 2015

Keywords:
Satellite altimetry
Microwave radiometer
Wet tropospheric correction
Objective analysis
GNSS

ABSTRACT

The wet tropospheric correction (WTC) is still a significant error source in most altimetric products. For studies such as sea level change, as those performed in the scope of the ESA Sea Level Climate Change Initiative (SL_cci) project, the use of uniform and consistent WTC datasets are of major importance. For this purpose, a set of improved WTC, using the Global Navigation Satellite System (GNSS) derived Path Delay (GPD) algorithm, was envisaged for the main six altimetric missions: the so-called reference missions (TOPEX/Poseidon, Jason-1 and Jason-2) and the three ESA missions (ERS-1, ERS-2 and Envisat).

The GPD methodology is based on the combination of wet path delays derived from zenith total delays calculated at a network of coastal GNSS stations and valid microwave radiometer (MWR) measurements at altimeter nearby points. At each altimeter point with an invalid MWR value, the WTC is estimated from the set of observations, along with the associated mapping error, using a linear space-time objective analysis technique that takes into account the spatial and temporal variability of the WTC field and the accuracy of each data set used. In the absence of observations, tropospheric delays from the European Centre for Medium-range Weather Forecasts (ECMWF) ReAnalysis (ERA) Interim model are adopted.

Originally designed to improve the WTC in the coastal zone, the GPD evolved to include the global ocean, correcting for land and ice contamination in the MWR footprint, or spurious measurements due to e.g. instrument malfunction.

This paper presents an overview of the GPD implementation for the afore-mentioned six altimetric missions.

The GPD products have been validated by comparison with the WTC adopted as the reference correction by the Archiving, Validation, and Interpretation of Satellite Data in Oceanography (AVISO): the so-called composite correction (Comp) for all missions except Jason-2, for which the version D of the Geophysical Data Records (GDR-D) Advanced Microwave Radiometer (AMR) WTC is adopted. Various sea level anomaly (SLA) statistical analyses have been performed and are summarised in this paper: differences in SLA variance calculated along satellite tracks and at crossovers; SLA variance difference function of distance from the coast or function of latitude.

Results show that the GPD WTC evidence a very significant improvement with respect to the Comp correction, particularly at polar and coastal regions, for all ESA and TOPEX/Poseidon missions. For the last, the impact is particularly significant in the second part of the mission, since detected anomalies present in the TOPEX Microwave Radiometer products are corrected by the algorithm. For Jason-1 and Jason-2, some improvements are observed in the coastal regions, although globally not very significant, particularly for Jason-2. This is attributed to the good performance of the WTC present in the most recent Jason-1 and Jason-2 products.

The GPD WTC constitutes a coherent dataset of global and continuous corrections, for most missions a major improvement with respect to the baseline MWR and the Comp wet tropospheric corrections.

© 2015 The Authors. Published by Elsevier Inc. This is an open access article under the CC BY-NC-ND license (http://creativecommons.org/licenses/by-nc-nd/4.0/).

1. Introduction

Observations of the ocean by remote sensing techniques are required for applications that extend beyond the direct exploitation of the ocean for economic and social purposes, including the monitoring of climate and the environment on seasonal-to-interannual-to-decadal time scale. Amongst the various remote sensing techniques, satellite radar altimetry plays a major role in the study of e.g. ocean circulation and sea level change at global and regional scales. At present, the nearly 22-year altimetric record is long enough to characterise the long-term sea level variability at inter-annual time scales.

Since the 1990s, several satellite altimetry missions have been providing a continuous, all weather, day and night set of observations, allowing an unprecedented number of studies with particular strong impacts over the ocean, inland water and polar regions:

* Corresponding author at: Univ. Porto, Faculdade de Ciências, Porto, Portugal.
E-mail address: mjfernan@fc.up.pt (M.J. Fernandes).

http://dx.doi.org/10.1016/j.rse.2015.07.023
0034-4257/© 2015 The Authors. Published by Elsevier Inc. This is an open access article under the CC BY-NC-ND license (http://creativecommons.org/licenses/by-nc-nd/4.0/).

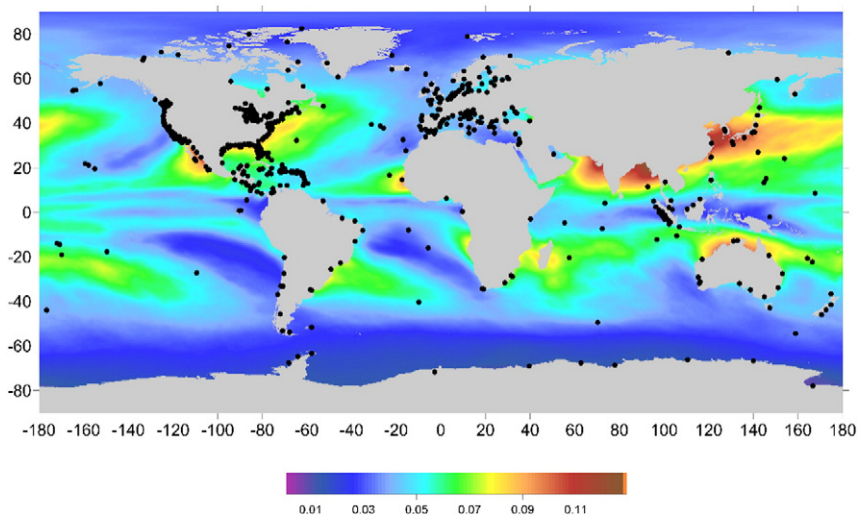

Fig. 1. Location of the global set of GNSS coastal and island stations (black dots) used in the GPD computations. The background picture is the map of the standard error of the wet tropospheric correction, in metres, computed from two years of ECMWF model fields.

Geosat (1985–1990), European Remote Sensing Satellite-1 (ERS-1, 1991–1995), TOPographic EXperiment/Poseidon (TOPEX/Poseidon, 1992–2005), ERS-2 (1995–2011), Geosat Follow-On (GFO, 1998–2008), Envisat (2002–2012), Jason-1 (2001–2013), Jason-2 (2008–present), CryoSat-2 (2010–present), HY-2A (Haiyang-2A) (2011–present) and SARAL (Satellite with ARgos and ALtiKa) (2013–present).

Future missions include Jason-3 (planned for 2015), Sentinel-3A (planned for 2016), Sentinel-3B (planned for 2017), Sentinel-6, Jason-CS (Jason Continuity of Service, planned for 2020) and SWOT (Surface Water and Ocean Topography, planned for 2020).

The orbits of these missions have been selected to allow different and complementary sampling of the Earth's surface. The missions developed by the consortia formed by NASA (National Aeronautics and Space Administration) and CNES (Centre National d'Études Spatiales) TOPEX/Poseidon and Jason-1 and their follow-on, Jason-2, developed jointly with the European Organisation for the Exploitation of Meteorological Satellites (EUMETSAT), the so-called reference missions, have a 10 day repeat cycle and 315 km inter-track spacing at the equator. The European Space Agency (ESA) missions, ERS-1 (only during part of the mission), ERS-2 and Envisat, have a 35 day repeat cycle and 80 km inter-track spacing at the equator. SARAL, a joint ISRO (Indian Space Research Organization) and CNES mission, carrying amongst other instruments, AltiKa, built by CNES, has an orbit coincident to that of Envisat. GFO had a 17 day repeat cycle and 163 km inter-track spacing at the equator. During part of the mission, Geosat was on an exact repeat orbit similar to that of GFO, the remaining period being on a geodetic orbit with a final inter-track spacing at the equator of 4 km. CryoSat-2 has a geodetic orbit with a 369 day repeat cycle and a sub-cycle close to 28 days. HY-2A is a satellite launched by CNSA (China National Space Administration) with a 14 day repeat cycle and 315 km inter-track spacing at the equator.

Precise sea surface height (SSH) measurements of 1–3 cm accuracy are now possible by means of improved tracking techniques of the radar echo, precise orbits and accurate modelling of all instrument, range and geophysical effects (Andersen & Scharroo, 2011; Chelton, Ries, Haines, Fu, & Callahan, 2001). Various range and geophysical corrections are required to account for the effects in the radar pulse and echo backscatter due to the interaction of the signal with the troposphere (dry and wet), the ionosphere, with the sea surface (sea state bias) and for geophysical phenomena (dynamic atmospheric correction, tides), which must be accounted for in order to separate them from the signals of interest. Amid these corrections, the delay due to the water vapour content in the troposphere, the wet tropospheric correction (WTC) is still considered one of the major sources of uncertainty.

In spite of its relatively low absolute value, less than 50 cm, but highly variable both in space and time, the precise modelling of this correction is still a challenge. Due to its high variability the most precise way to

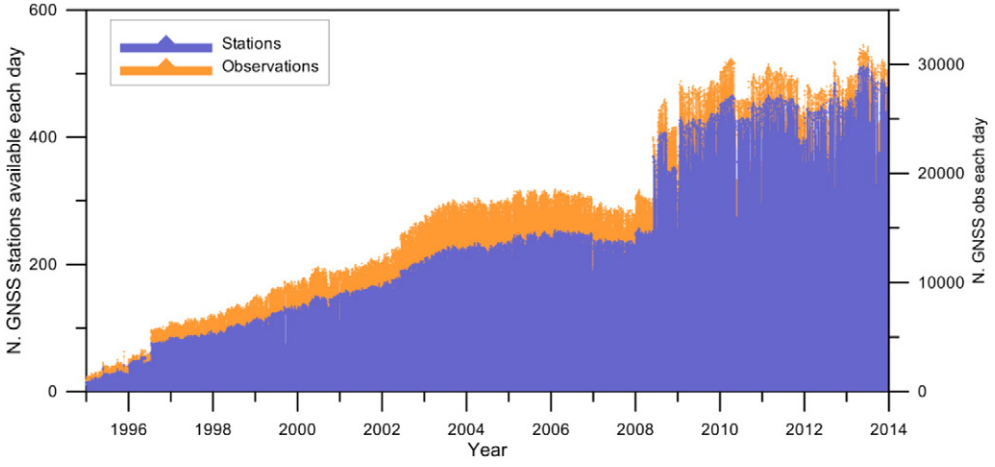

Fig. 2. Number of GNSS stations (blue) and number of GNSS measurements available per day since 1995.

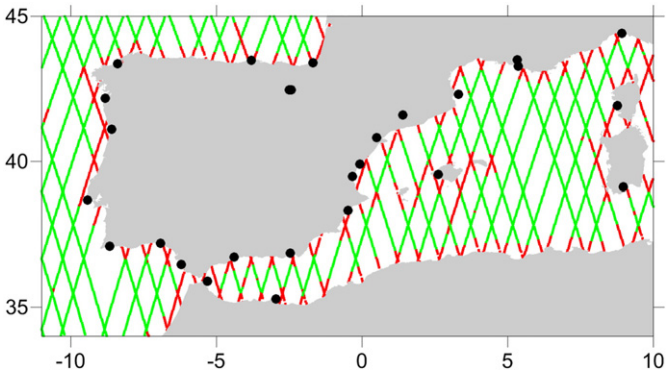

Fig. 3. Location of all data sets selected for the GPD computation for Envisat cycle 62: green — Envisat points with valid MWR data; red — Envisat points with invalid MWR data; black — GNSS stations (see text for details).

derive this correction is through collocated measurements made by microwave radiometers (MWR) on board the altimetric missions.

Two main types of nadir-looking radiometers have been deployed in the altimetric satellites: 2-band in ERS-1, ERS-2, Envisat, GFO, SARAL and upcoming Sentinel-3; 3-band on TOPEX/Poseidon, Jason-1 and Jason-2. All of them have one band in the water vapour absorption line between 21 and 23.8 GHz plus one or two in "atmospheric window" channels. The "window" channels are required to account for the effect of surface emissivity and for the cloud scattering.

The 2-band radiometers have the second band in the 34–37 GHz window, sensitive to surface emissivity and also sensitive to cloud liquid water; the 3-band radiometers have a third channel near the 18–18.7 GHz band, also sensitive to surface emissivity and with particularly low sensitivity to clouds, improving the retrieval of the atmospheric correction (Brown, 2010; Eymard & Obligis, 2006). In the 2-band microwave radiometers, which do not include the low frequency channel, the surface roughness is taken into account through the altimeter derived wind speed or the backscatter coefficient. The footprint of these instruments is of the order of 20–45 km depending on the instrument and frequency (Tournadre, 2006) except for AltiKa on board SARAL, which is about 10 km (Tournadre, Lambin-Artru, & Steunou, 2009; Verron & Steunou, 2006). For example, the Advanced Microwave Radiometer (AMR) on board Jason-2 has twice the spatial resolution of its predecessors, the Topex Microwave Radiometer (TMR) and Jason-1 Microwave Radiometer (JMR) (Brown, 2010).

More precisely, the 2-band radiometer on-board the ESA missions is a noise injection radiometer operating at 23.8 and 36.5 GHz (Bernard, Le Cornec, Eymard, & Tabary, 1993; Obligis, Eymard, Tran, Labroue, & Femenias, 2005). TMR performs measurements at 18, 21 and 37 GHz (Ruf, Keihm, & Janssen, 1995) and JMR and AMR at 18.7, 23.8 and 34.0 GHz (Brown, Ruf, Keihm, & Kitiyakara, 2004).

The algorithms used to retrieve the WTC from the measured brightness temperatures of the various MWR channels assume a constant surface ocean emissivity and are valid for ocean conditions, light rain and wind speed lower than 20 $m \cdot s^{-1}$. Therefore, in the presence of surfaces with different emissivity, such as land or ice, the measurements become invalid. Thus, in spite of the high accuracy of MWR-derived WTC in open-ocean, hampered by the contamination from land, ice and rain in the radiometer footprint, the correction may be highly degraded, particularly in coastal and polar regions (e.g. Andersen & Cheng, 2013; Cheng, Andersen, & Knudsen, 2015). Consequently, most current altimeter products fail to provide valid MWR-derived WTC in these regions. In addition, noisy values caused by instrumental problems, jumps and drifts may also occur in one or more channels, e.g., Scharroo, Lillibridge, Smith, and Schrama (2004).

A number of approaches have been proposed for correcting the altimeter measurements in the coastal regions, where the MWR measurements become invalid due to land contamination in the radiometer footprint.

In the last years, four main approaches have been proposed: (1) Land Contamination Algorithm (LCA); (2) Mixed-Pixel Algorithm (MPA); (3) GNSS (Global Navigation Satellite System) derived Path Delay (GPD) approach; and (4) Dynamically-Linked Model (DLM) approach.

The first method (LCA) has been implemented to Jason-2 data in the scope of project PISTACH (Desportes, Obligis, & Eymard, 2007; Obligis, Rahmani, Eymard, Labroue, & Bronner, 2010). The second one (MPA) has been developed at the Jet Propulsion Laboratory (JPL, USA), first applied to Jason-2 data (Brown, 2010) and later to Jason-1. The third method (GPD) was first developed by University of Porto (U.Porto) in the scope of the European Space Agency (ESA) project COASTALT (Development of radar altimetry data processing in the oceanic coastal zone) for the generation of Envisat Coastal Geophysical Data Records (CGDR) (Fernandes et al., 2010). The fourth method (DLM) was first used by Fernandes, Bastos, and Antunes (2003) and has been implemented in COASTALT (COASTALT, 2009; Obligis et al., 2011). A similar approach, the composite correction, has been used by Mercier (2004) and Mercier, Rosmorduc, Carrere, et al. (2010) and is being implemented in the Archiving, Validation, and Interpretation of Satellite Data in Oceanography (AVISO) products.

Amid these methods, the GNSS-derived path delay algorithm, developed by U.Porto, improves data retrieval not only near the coast, but also in open-ocean, by correcting the baseline MWR-derived WTC from other sources of error. In the scope of COASTALT, the method was first applied, just as a coastal algorithm, in the SW European region for the whole Envisat data series (Fernandes et al., 2010) and was later extended, in the scope of ESA Sea Level Climate Change Initiative (SL_cci) project (Ablain et al., 2015; Larnicol et al., 2012), to the global data sets of the main altimetric missions.

The SL_cci project aims to produce and validate the Sea Level Essential Climate Variable (ECV) product, one of the 50 Essential Climate Variables (ECVs) listed by the Global Climate Observing System (GCOS) in climate change monitoring. For this purpose, the best algorithms for climate applications are being developed, tested and selected.

As part of this work, aiming to provide a uniform WTC for all missions, an improved WTC dataset, using the GPD methodology, has been developed for the six main altimetric missions and was selected for use in the generation of the first version of the sea level ECV products ERS-1 (E1), ERS-2 (E2), Envisat (EN), Topex/Poseidon (TP), Jason-1 (J1) and Jason-2 (J2).

The GPD WTC constitutes a coherent dataset of global and continuous corrections, for most missions a major improvement with respect to the baseline MWR WTC.

This paper presents the results of the GPD implementation for the six main altimetric missions: the reference missions TOPEX/Poseidon, Jason-1 and Jason-2, and the ESA ERS-1, ERS-2 and Envisat missions.

Section 2 describes the main aspects of the GPD algorithm: the objective analysis (OA) implementation and data sets used. Section 3 presents the main characteristics of the GPD WTC products for each mission. The results were validated by a set of statistical analyses of sea level anomaly (SLA) variances, presented in Section 4. Section 5 summarises the main conclusions and future prospects.

2. The GPD algorithm

2.1. OA implementation

The GPD methodology is based on the combination, by objective analysis (OA), of wet path delays from various sources: valid microwave radiometer (MWR) measurements at the nearby points, zenith wet delays (ZWD) derived from GNSS datasets and tropospheric delays derived from atmospheric models.

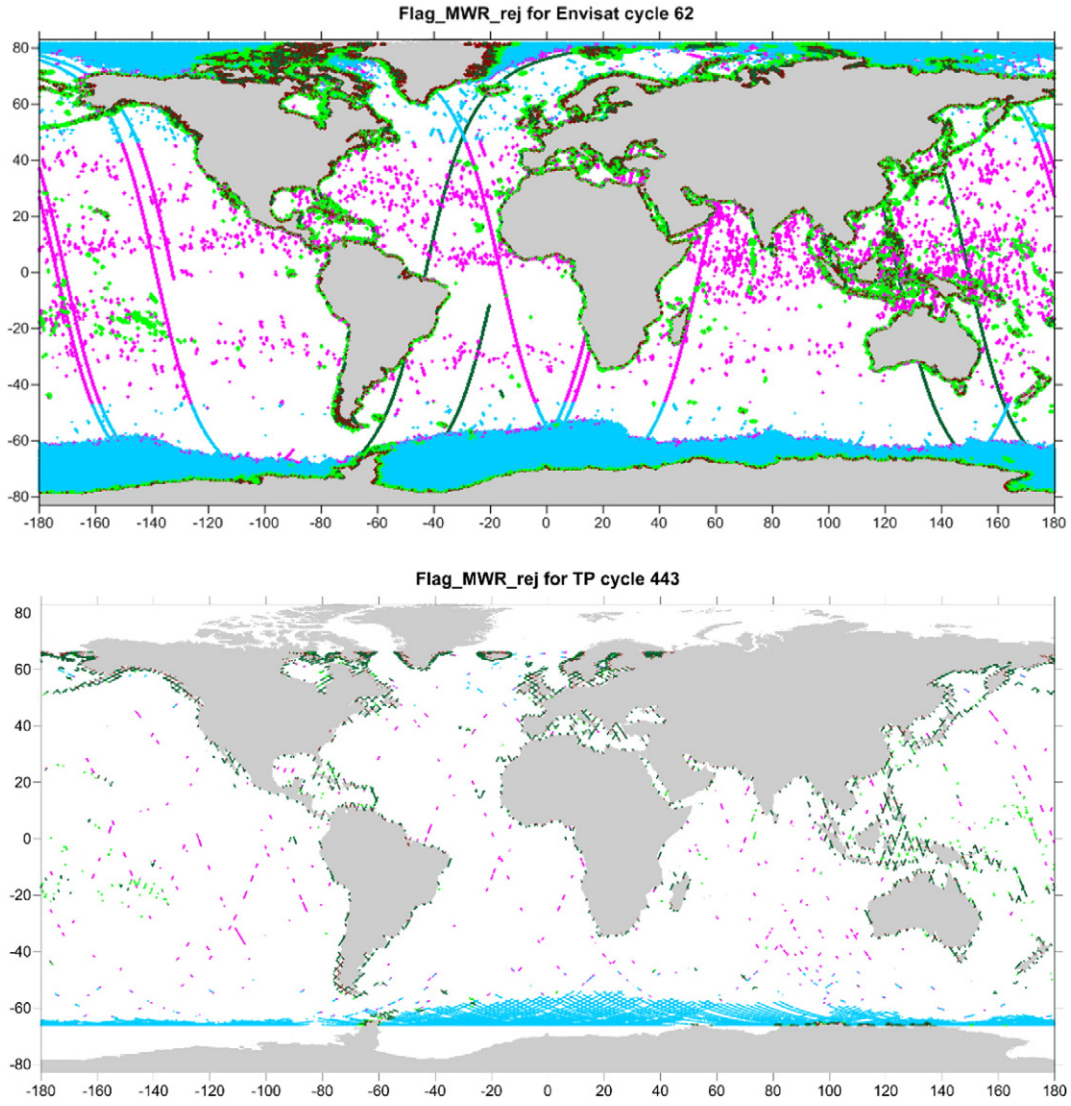

Fig. 4. Location of Envisat cycle 62 (top) and TP cycle 443 (bottom) points selected for the GPD computation (points with flag_MWR_rej ≠ 0). Dark green: points with radiometer land flag set to 1; light green: points with distance from coast less than a given threshold; blue: points contaminated by ice; pink: points rejected by outlier detection criteria or with the MWR WTC outside limits; brown: land points near the coast (see text for details).

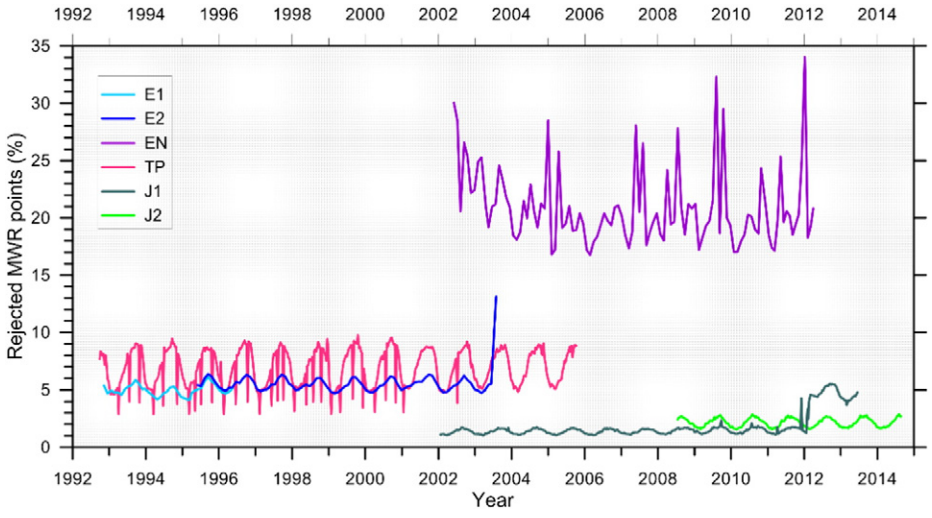

Fig. 5. Percentage of invalid MWR points selected for estimation of the WTC by the GPD algorithm for each cycle of the six altimetric missions.

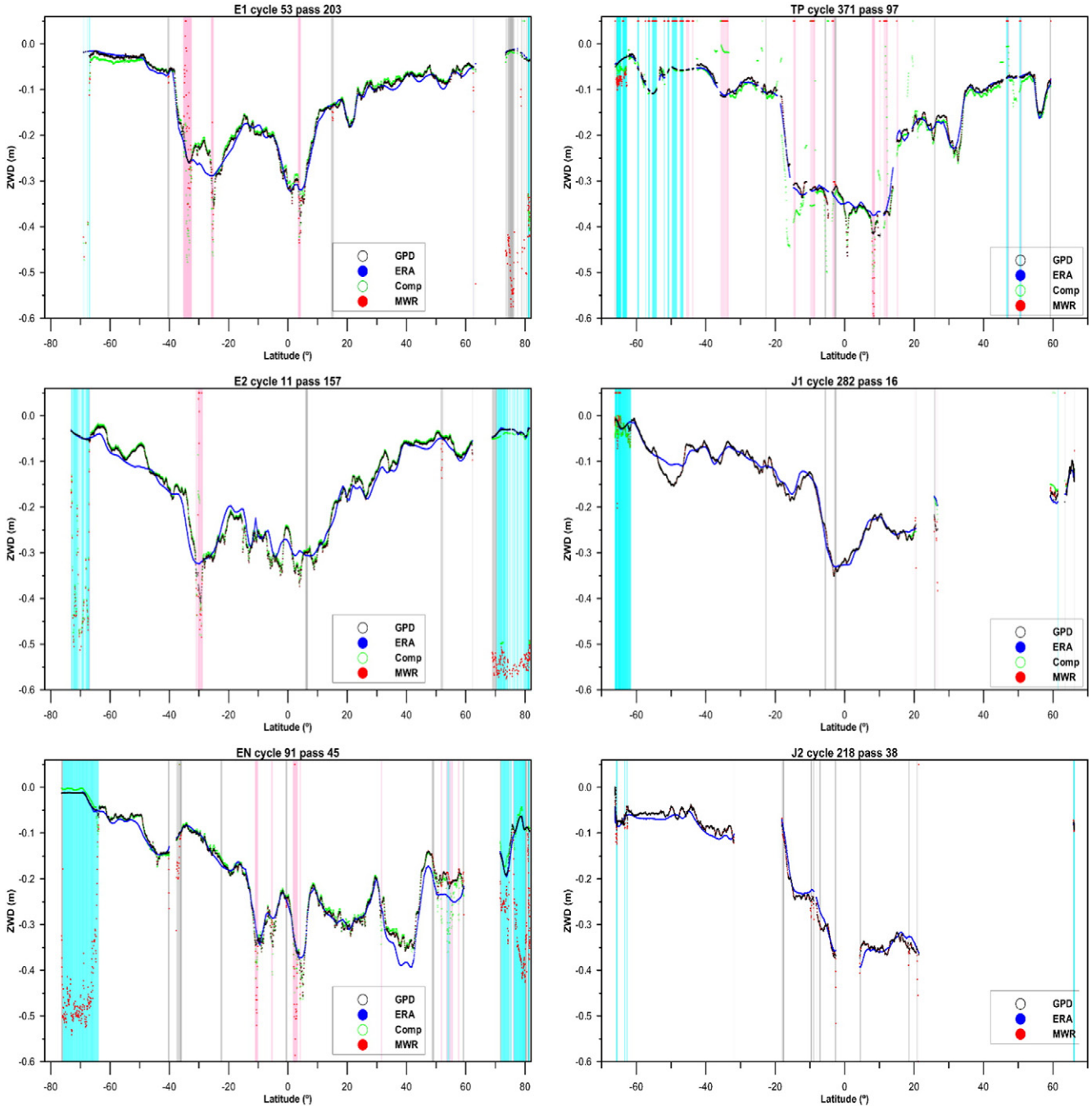

Fig. 6. Examples of plots along passes of the six altimetric missions: a) ERS-1; b) ERS-2; c) Envisat; d) T/P; e) Jason-1; f) Jason-2. The GPD wet tropospheric correction (black) is shown against the base MWR (red), ERA Interim (blue) and Composite (green). Shaded areas represent invalid MWR points for which a new GPD estimated is obtained: grey — land contaminated regions; cyan — ice contaminated regions; pink — points rejected by other causes, e.g. instrumental problems. Outside the bars the red MWR points cannot be observed since they are under the black points, i.e., on these points the GPD equals the baseline MWR correction.

At each altimeter point with an invalid MWR value, the GPD estimates the wet tropospheric correction, along with the associated mapping error, using a linear space-time objective analysis (i.e., optimal interpolation) technique (Bretherton, Davis, & Fandry, 1976). The underlying method, previously developed for coastal altimetry and described in Fernandes et al. (2010), uses the wet path delay observations to update a first-guess WTC value known a priori at each location and epoch and provides a quantification of the mapping error associated with each estimated WTC value. Full details of the OA method can be found in Bretherton et al. (1976), here only a simplified description is given.

The estimate of the WTC field at each along-track point P, F(P), is given by a "first guess", FG(P), plus a weighted average of the set of N WTC anomalies X_i^{ano} (Eq. (1)), computed subtracting the first guess from the N WTC observations X_i (Eq. (2)) within given space and time search radiuses around point P:

$$F(P) = FG(P) + \sum_{i=1}^{N} W_i \; X_i^{ano} \tag{1}$$

$$X_i^{ano} = X_i - FG(P). \tag{2}$$

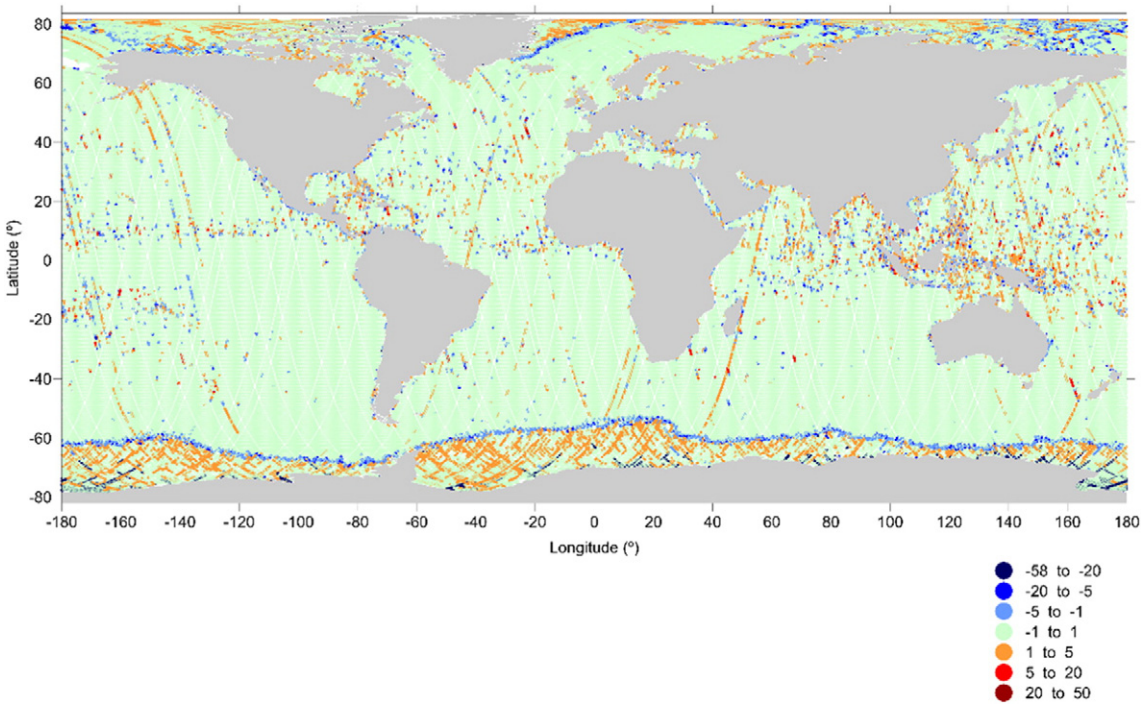

Fig. 7. Difference between the Composite and GPD wet tropospheric corrections for Envisat cycle 62, in centimetres.

The weights W_i are estimated from the statistical properties of the WTC field:

$$W_i = \sum_{k=1}^{N} C_k \; A_{ik}^{-1} \tag{3}$$

where C_k is the covariance between the estimation point P and the nearby measurement point k, k = 1,...,N, and A_{ik}^{-1} is the inverse of the variance–covariance matrix of the WTC measurements. Each covariance is normalized by dividing by the variance of the WTC field at the estimation point P, so in fact correlations instead of covariances are used.

In practice, the covariance between each pair of points separated by a distance r and time difference Δt is computed from a correlation function. Thus, the spatial and temporal variability of the WTC field is taken into account by the correlation function. In the absence of the knowledge of an empirical covariance model of the background field, the

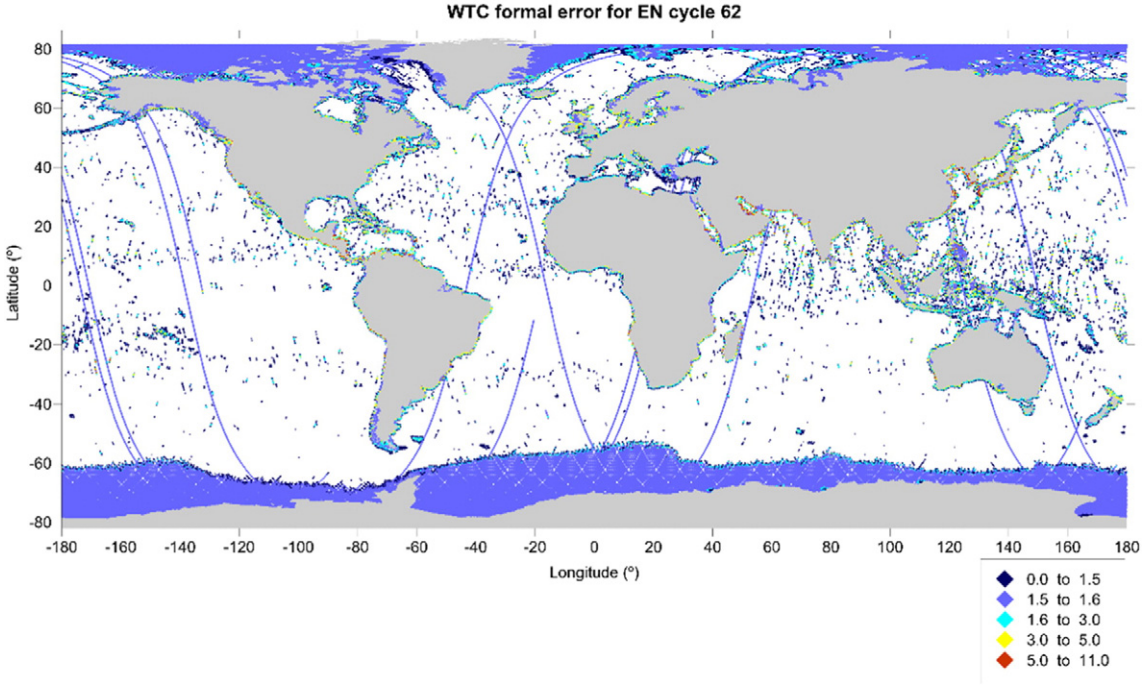

Fig. 8. Formal error (in cm) of the GPD wet tropospheric correction for Envisat cycle 62.

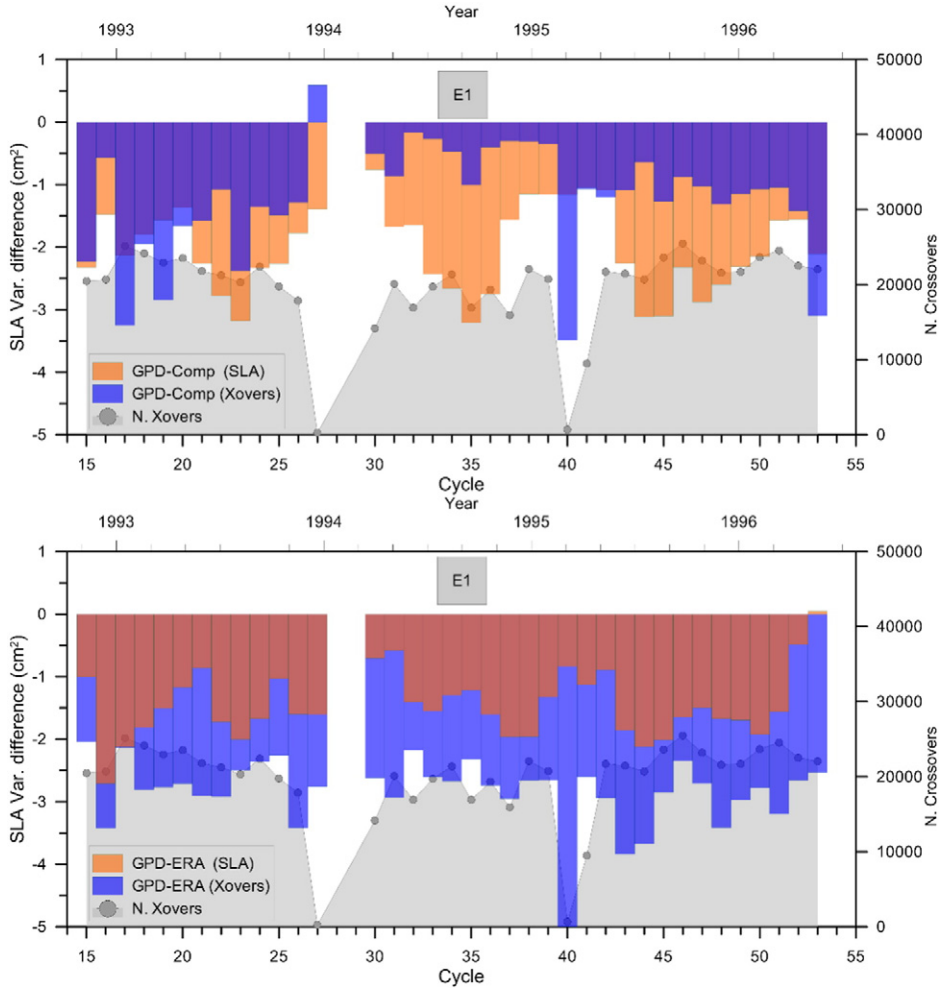

Fig. 9. Temporal evolution of weighted SLA variance differences along track (orange) and at crossovers (blue) between GPD and Comp (top) and ERA (bottom) over the period of E1 cycles 15 to 53 (AVISO convention), spanning phases c, e, f and g (1992.8–1996.4). "N. Crossovers" represents the number of crossovers per cycle.

correlation function $F(r,\Delta t)$ can take the form of a product of two stationary Gaussian decays (Leeuwenburgh, 2000; Schüler, 2001), i.e.,

$$F(r,\Delta t) = F_r(r) \times F_{\Delta t}(\Delta t) = e^{-\frac{r^2}{D}} \times e^{-\frac{\Delta t^2}{T}} \quad (4)$$

where r is the distance and Δt is the time interval between acquisition of each pair of points, and D and T are the spatial and temporal correlation scales, respectively.

In summary, the implementation of the method requires the knowledge of the following quantities:

- First guess of *WTC*;
- Variance of the *WTC* field;
- White noise associated with each *WTC* data set (required to compute the diagonal elements of the variance–covariance matrix, A_{ik});
- Parameters defining the correlation function: space and time correlation scales;
- Space and time search radii.

The first guess is the WTC from the European Centre for Medium-range Weather Forecasts (ECMWF) ReAnalysis (ERA) Interim model, centred at the location and instant of the altimeter measurement at which the estimation is required. In this way, in the absence of any type of observations, the estimate will be the first guess, i.e., the model-derived WTC.

The variance of the WTC field was determined from a 2-year dataset of the ECMWF operational model (2013–2014) at 0.125° × 0.125° and 6-hour intervals. The square root of the variance of the field, i.e., its standard deviation, is represented in Fig. 1.

For the white noise associated to each data type the following values were adopted: GNSS: 0.5 cm (Fernandes, Nunes, & Lázaro, 2013a; Fernandes, Pires, Lázaro, & Nunes, 2013b; Fernandes et al., 2010); MWR: 0.5 cm.

Following Bosser, Bock, Pelon, and Thom (2007), spatial and temporal scales of 100 km and 100 min, respectively, have been initially adopted. The present implementation uses a latitude dependent spatial correlation scale. The data used for each WTC estimation are the WTC values from all data sets within the spatial and temporal influence regions, centred at the location and instant of the altimeter measurement at which the estimation is required; those ranges should equal the spatial and temporal correlation scales.

The main difference of the present implementation with respect to that presented in Fernandes et al. (2010) is that while in Fernandes et al. (2010) the model-derived WTC were also combined with the actual observations, now the model-derived WTC is only used as first guess

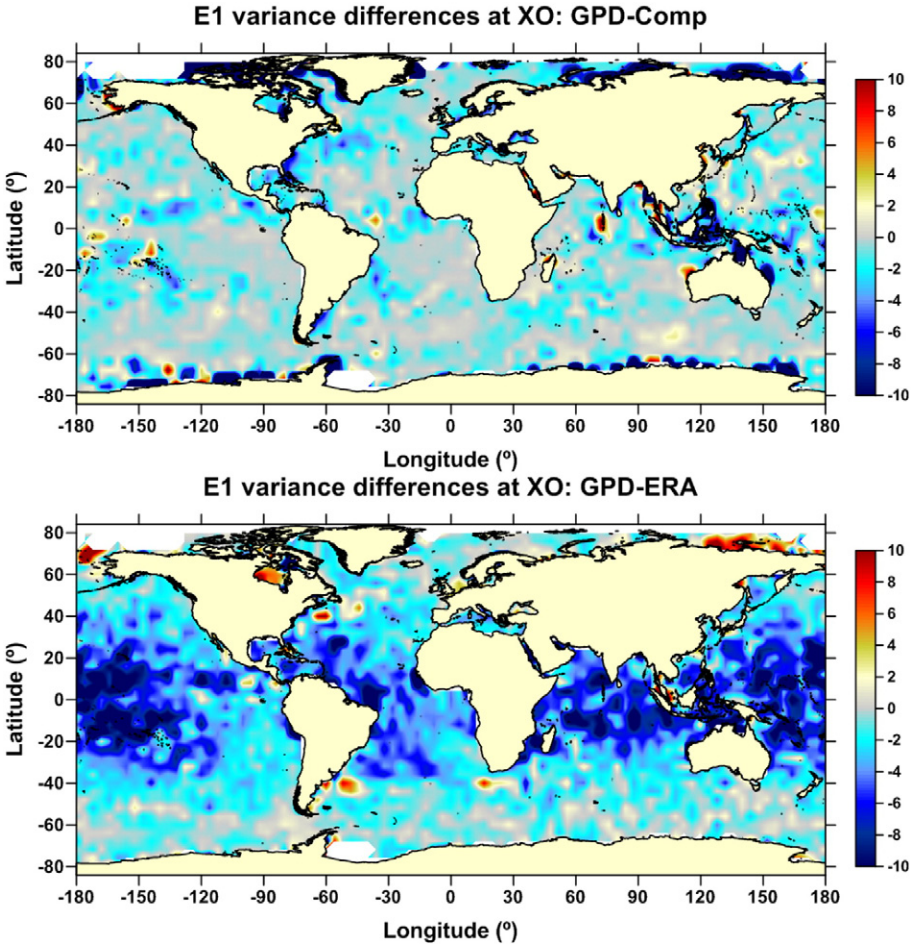

Fig. 10. SLA variance differences at crossovers between GPD and Comp (top) and ERA (bottom) over the period of E1 cycles 15 to 53 (AVISO convention), spanning phases c, e, f and g (1992.8–1996.4).

in the OA procedure. The first approach led to slightly smoother estimates, while the second leads to estimates solely based on observations (provided they exist) and smaller formal errors.

2.2. Data sets

The data types used in the GPD algorithm, described in the following sub-sections, are:

- Zenith wet delays derived at a network of coastal and island GNSS stations;
- WTC from valid microwave radiometer measurements at points in the vicinity of the estimation point;

In addition, WTC from a Numerical Weather Model (NWM) such as the ERA Interim model are used.

2.2.1. Radar altimeter and MWR data

For each mission, the adopted baseline WTC from the on-board MWR is the correction present in the Radar Altimetry Database System (RADS), status in 2014, except for Envisat for which the latest correction, Version 2.1b, has been used. The reason for adopting the MWR-based WTC available in RADS is because RADS provides the most complete, harmonized altimetric data set, including a wide collection of state-of-the-art range and geophysical corrections and e.g. orbit solutions, mean sea surface (MSS), geoid models and topographic/bathymetric models (Scharroo et al., 2012), which facilitates the extraction of the various fields required not only in the WTC estimation but also in the validation tasks.

In summary, the following MWR data sets were used:

- ERS-1 and ERS-2 — MWR data are based on the ESA Ocean Product (OPR) modified by the algorithms discussed in Scharroo et al. (2004);
- Envisat — MWR version V2.1b, a recent correction provided by CLS (CLS internal technical note: Reprocessing of RA2-MWR v2.1b. CLS-DOS-NT-13-114);
- TOPEX/Poseidon — Topex Microwave Radiometer (TMR) replacement product (http://podaac.jpl.nasa.gov/dataset/TOPEX_L2_OST_TMR_Replacement);
- Jason-1 — a new JMR product provided by S. Brown (Remko Scharroo, personal communication), already enhanced near the coast (Brown, 2010);
- Jason-2 — AMR GDR-D product, already enhanced near the coast, Brown (2010).

The Composite (Comp) correction, adopted as reference in the AVISO products, has been taken from the SL_cci database Version 1. The Composite Correction is a conceptually simple method, which consists in replacing the MWR measurements near the coast (<50 km) by ECMWF model values. The ECMWF correction is shifted to the nearest valid radiometer measurement in the transition zone. Interpolation and detrending are also applied in complex cases (Mercier et al., 2010).

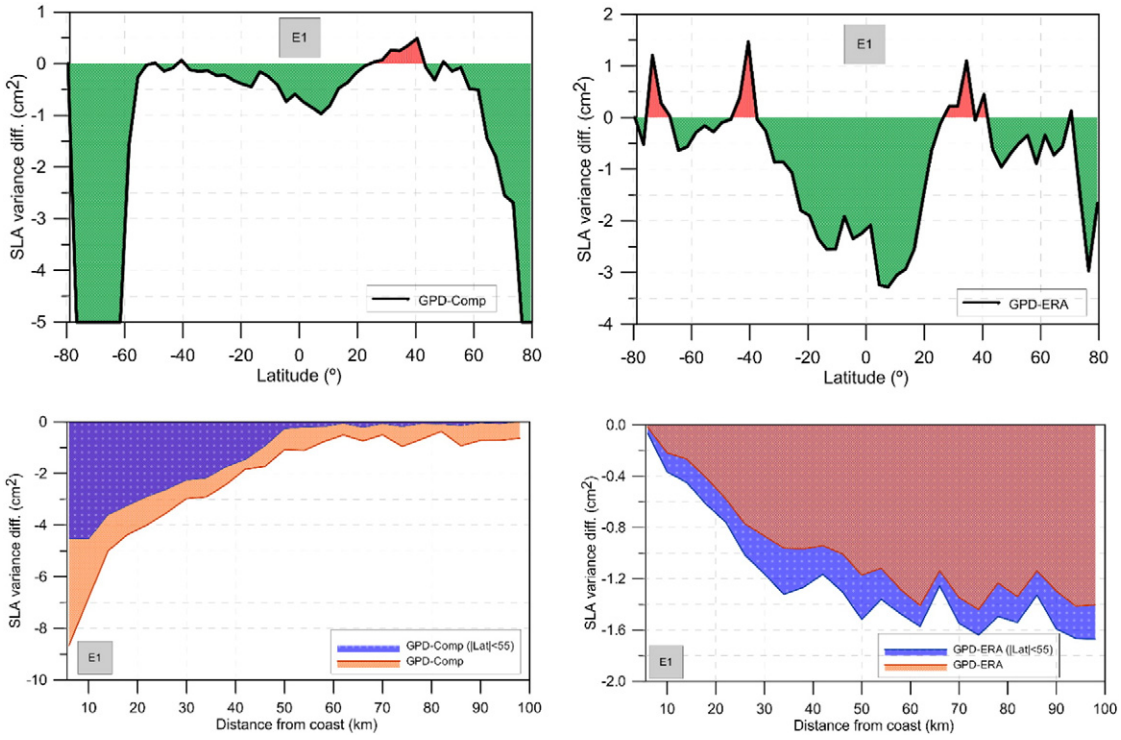

Fig. 11. Variance differences of SLA versus latitude (top) and distance from coast (bottom) between GPD and Comp (left) and ERA (right) for E1 cycles 15–53 (AVISO convention (1992.8–1996.4). In the bottom panels the orange and blue plots represent the results for the whole range of latitudes and for the latitude band $|\varphi| < 55°$, respectively.

2.2.2. GNSS data

At present, the determination of zenith total delays (ZTD) at GNSS stations makes use of well-established methodologies, allowing the determination of ZTD at the station location with an accuracy of a few millimetres (Fernandes, Nunes, & Lázaro, 2013a; Fernandes et al., 2010; Niell et al., 2001; Pacione et al., 2011; Snajdrova, Boehm, Willis, Haas, & Schuh, 2006).

The tropospheric propagation delay is modelled in GNSS processing as:

$$\mathrm{STD}(E) = \mathrm{ZHD}\ \ \mathrm{mf_h}(E) + \mathrm{ZWD}\ \ \mathrm{mf_w}(E) \tag{5}$$

where STD is the measured slant total delay, E is the elevation angle of the GNSS satellite and $\mathrm{mf_h}$ and $\mathrm{mf_w}$ are the mapping functions for hydrostatic and wet components, respectively.

In Eq. (5), a priori zenith hydrostatic delay (ZHD) is evaluated from available surface pressure using the modified Saastamoinen model (Davis, Herring, Shapiro, Rogers, & Elgered, 1985) and $\mathrm{mf_h}$ and $\mathrm{mf_w}$ are known mapping functions relating the zenith delays with those in the slant direction.

The most important factors in the ZTD estimation are the a priori ZHD used in Eq. (5) (Kouba, 2009; Tregoning & Herring, 2006), the dry and wet mapping functions, and the use of an appropriate cut-off elevation angle (~7°). The most commonly used mapping functions are the Global Mapping Functions (GMF) (Boehm, Niell, Tregoning, & Schuh, 2006b) and the Vienna Mapping Functions 1 (VMF1, Boehm, Werl, & Schuh, 2006a), the latter leading to higher accuracy.

Various software packages are available for this computation, e.g. GAMIT (Herring, King, & McClusky, 2006), GIPSY/OASIS (Zumberge, Heflin, Jefferson, Watkins, & Webb, 1997) and Bernese (Dach, Brockman, & Schaer, 2009; Dach, Hugentobler, Fridez, & Meindl, 2007). In GAMIT the computations are performed using double differences phase measurements for sets of stations on a global network, since when using a small regional network all stations observe the same satellite with similar viewing angles and the corresponding zenith delays will be highly correlated. Both GIPSY/OASIS and Bernese allow the use of the Precise Point Positioning (PPP) technique, which performs the processing of each station separately, thus avoiding the calculation on a global network as required by the GAMIT software.

From Eq. (5), for each observation, a combined ZTD value is obtained, as the sum of the a priori ZHD and the estimated ZWD. In principle, an error in the a priori ZHD will be absorbed by the estimated ZWD. Thus, the quantity precisely estimated at each GNSS station is the total tropospheric correction (ZTD) at station level. The quantity used in coastal altimetry is the ZWD or WTC at sea level. This is obtained from the ZTD at station level by subtracting the dry tropospheric correction (DTC) or zenith hydrostatic delay at station level, followed by the ZWD reduction to sea level.

Since ZHD and ZWD have significantly different height dependence, their separation is a crucial step and their height dependence must be modelled separately.

Studies performed by Fernandes, Pires, Lázaro, and Nunes (2013b), on a set of GNSS coastal sites with heights up to 1000 m, show that the DTC (or ZHD) can be computed, at a surface point, with accuracy of a few mm from sea level pressure (SLP) fields from an atmospheric model such as ERA Interim or ECMWF operational, using the modified Saastamoinen model (Davis et al., 1985, Eq. (6)), further reduced to surface height using an adequate model for the height dependence of atmospheric pressure such as the one given by Hopfield (1969), Eq. (7).

$$ZHD = -\frac{0.0022768\ \ p_s}{1-0.00266\cos 2\varphi - 0.28\cdot 10^{-6}\ \ h_s} \tag{6}$$

$$p_s = p_0\ \ \exp\left[-\frac{g_m(h_s-h_0)}{RT_m}\right] \tag{7}$$

In Eq. (6), p_s is the surface pressure in hPa, φ is the geodetic latitude, h_s is the surface height above the geoid (in metres) and *ZHD* results in metres.

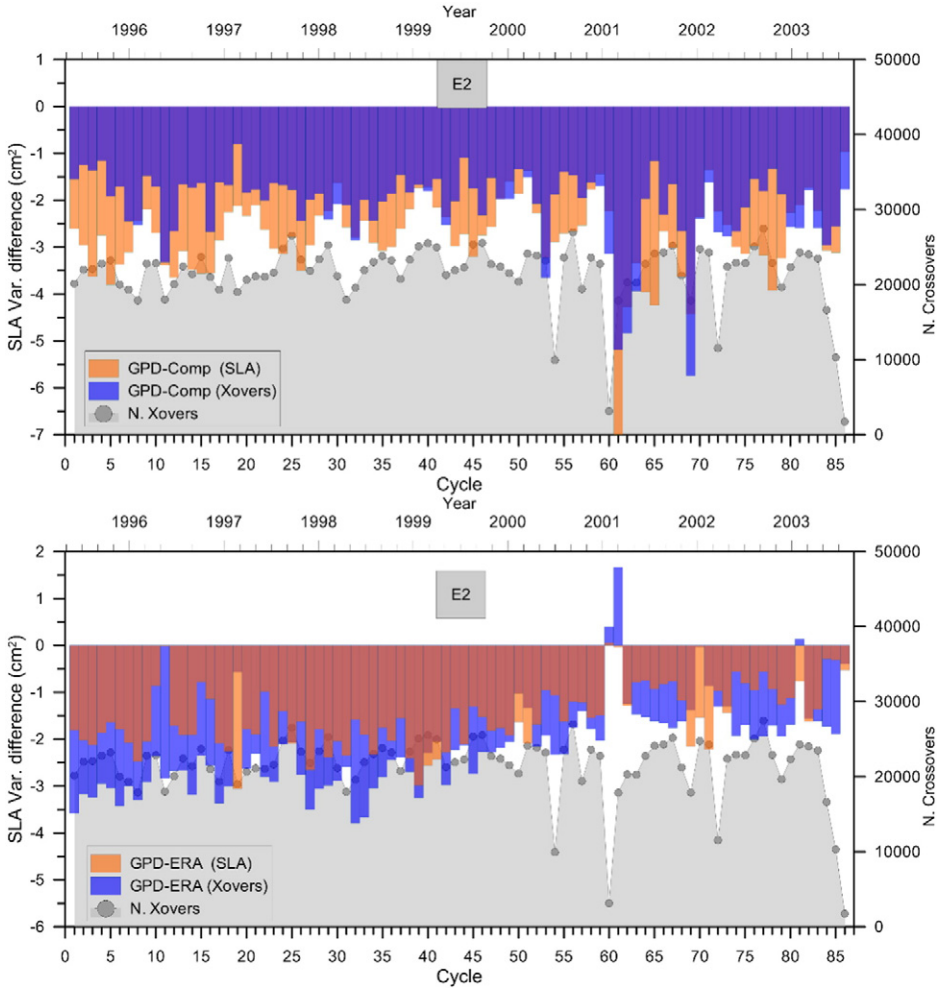

Fig. 12. Temporal evolution of weighted SLA variance differences along track (orange) and at crossovers (blue) between GPD and Comp (top) and ERA (bottom) over the period of E2 cycles 1 to 86 (1195.4–2003.6). "N. Crossovers" represents the number of crossovers per cycle.

In Eq. (7), p_0 is the sea level pressure, R is the specific constant for dry air (287.053 $J \cdot K^{-1} \cdot kg^{-1}$), T_m is the mean temperature (in K) of the layer between heights h_0 and h_s and g_m is the mean gravity, as given by:

$$g_m = 9.784\left(1-0.00266\cos 2\varphi - 0.28\cdot 10^{-6}\ h_s\right). \quad (8)$$

T_m can be estimated as the mean value of temperatures T_0 and T_s at heights h_0 and h_s, respectively, obtained, for example, from the values of T_0 at mean sea level given by the Global Pressure and Temperature (GPT) model (Boehm, Heinkelmann, & Schuh, 2007) and considering a value of $-0.0065\ K \cdot m^{-1}$ for the normal lapse rate of temperature with height.

Fernandes, Pires, Lázaro, and Nunes (2013b) also showed that the use of simplified expressions for the height dependence of atmospheric pressure such as the one by Berg (1948) will induce seasonal signals with amplitudes of several millimetres, due to the seasonal variation of pressure with temperature.

Unlike DTC, which has a relatively well-known height dependence, the height dependence of water vapour is not easy to model, due to its large variability. In spite of this, Kouba (2008) proposed the following empirical expression:

$$ZWD(h_s) = ZWD(h_0)e^{\frac{h_0-h_s}{2000}} \quad (9)$$

where h_S and h_0 are the ellipsoidal heights of the GNSS station and sea surface, respectively. Thus, height differences of, e.g., 100 and 500 m will induce ZWD differences of 5% and 28%, respectively (1 cm and 5.6 cm for a ZWD of 20 cm). For this reason, only stations up to 30 km from the coast and with orthometric height < 1000 m have been considered in this study (Fernandes, Pires, Lázaro, & Nunes, 2013b).

The GNSS data used in this study include zenith total delays computed at U.Porto and ZTDs available online at a set of IGS (International GNSS Service), at EPN (EUREF Permanent Network), SuomiNet stations and from sets of stations from a few regional networks (Figs. 1 and 2).

Fig. 2 shows that GNSS data availability is not uniform throughout the period of the various missions. Considering only coastal stations, it starts in 1995 with around 20, increasing continuously up to an average number of about 450 stations per day in 2014. The total number of coastal stations available for the GPD computations during the period [1992–2014] is close to 700, with a non-uniform spatial distribution (Fig. 1). While regions such as North America and Europe have a good coverage, the South America and African coasts have a small number of stations.

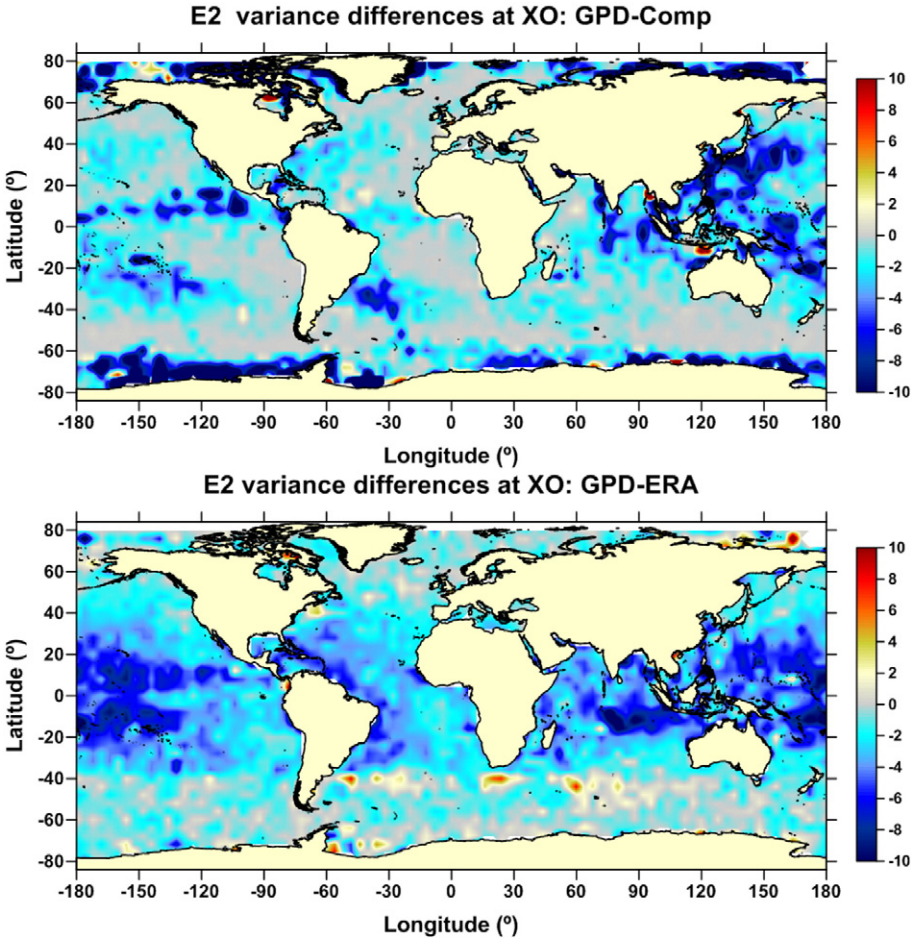

Fig. 13. SLA variance differences at crossovers between GPD and Comp (top) and ERA (bottom) over the period E2 cycles 1 to 86 (1195.4–2003.6).

Fig. 3 illustrates the spatial distribution of the two data sets (MWR and GNSS) in the region of southwest Europe.

2.2.3. Atmospheric model

ECMWF provides two main models for use in the estimation of tropospheric path delays, both providing global grids of several atmospheric parameters every 6 h, with different spatial resolution: the operational model (0.125° × 0.125°) and ERA Interim (0.75° × 0.75°) (Dee et al., 2011; Miller et al., 2010).

It is known that the ECMWF operational model does not provide a consistent climatological data record, as its several updates resulted in a number of discontinuities over time. Therefore, and in spite of the better spatial resolution of the operational model, for long-term studies involving the period prior to 2004, ERA Interim is a better option (Fernandes, Lázaro, Nunes, & Scharroo, 2014; Fernandes, Nunes, & Lázaro, 2013a; Legeais, Ablain, & Thao, 2014), being adopted in the computations of the GPD corrections. However, in the computation of the signal variance of the WTC field, the most recent version of the operational model at its highest spatial resolution has been used.

In the scope of this study, the atmospheric fields of three single-level parameters of the ERA Interim model were used for the period [1992–2015] and for the whole globe:

- Sea level pressure (SLP);
- Surface temperature (2-metre temperature, 2T);
- Total column water vapour (TCWV).

For each grid point, the WTC was computed at the ERA orography level, from the parameters TCWV and 2T and, only for land points, further reduced to sea level (Fernandes et al., 2010). The formula presented by Bevis et al. (1994) was adopted for the computation of the WTC from TCWV, in which the mean temperature of the troposphere was modelled from 2T according to Mendes, Prates, Santos, and Langley (2000). In the reduction to sea level Eq. (9) was used (Kouba, 2008). Further details can be found in Fernandes et al. (2014).

The WTC at each node of the ERA Interim model is used to estimate the model-derived WTC at the estimation point by bilinear interpolation in space and time, from the two closest model grids. The ERA Interim WTC values computed in this way are very similar to those present in the RADS products. Thus, when using RADS data, this computation is not required and the ERA WTC values present in RADS can be adopted instead. As mentioned above, the model-derived WTC at each estimation point is adopted as the first guess used in the OA implementation.

The SLP fields are used to compute the ZHD fields required in the processing of the GNSS data, as described in Section 2.2.2

2.3. Selection of invalid MWR values

Originally designed to estimate improved WTC values in coastal areas, where a set of GNSS inland stations can be found, the GPD algorithm was later extended to open ocean. An estimate is obtained for every ocean point along the altimeter ground track for which the WTC computed from the on-board MWR measurements has been considered

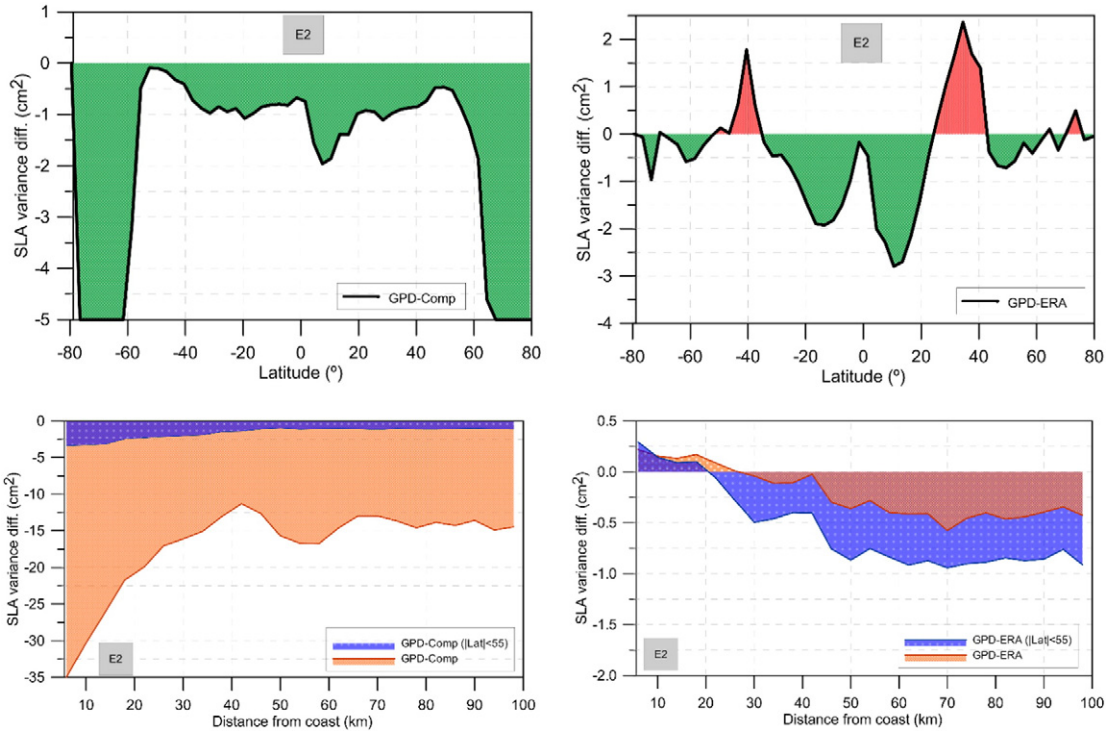

Fig. 14. Variance differences of SLA versus latitude (top) and distance from coast (bottom) between GPD and Comp (left) and ERA (right) for E2 cycles 1 to 86 (1195.4–2003.6). In the bottom panels the orange and blue plots represent the results for the whole range of latitudes and for the latitude band $|\varphi| < 55°$ respectively.

invalid. The validity of an MWR measurement is set by an MWR rejection flag (flag_MWR_rej) according to pre-defined criteria. A non-exhaustive list of such criteria is given below.

1) The radiometer surface type flag is on (rad_surf_type_flag = 1). In most missions this flag is only set over land and allows tracking most land-contaminated points near the coast. Sometimes it is also set for points with a default or NaN value, for example for a set of passes with invalid MWR values (see dark green points in Fig. 4).
2) The radiometer quality interpolation flag is not 0 (rad_qual_interp_flag ≠ 0). This is only used for Envisat and was particularly useful in previous MWR versions, in the detection of points near the coast where the last MWR value was extrapolated. In the V2.1b product this flag is not provided. Here the contaminated MWR values are given unchanged (light green points in Fig. 4).
3) The point is at a distance from coast less than a specified threshold (30 km for all ESA missions and TP; 15 km for J1 and J2). This criterion helps to spot any remaining land contaminated points not flagged by the previous criteria (light green points in Fig. 4).
4) Point is contaminated by ice. Ice contamination is detected by a set of criteria which are mission dependent. Examples of some of these criteria are: points for which the altimeter ice flag is set; the radiometer ice flag is set; the absolute difference between MWR WTC (wet_MWR) and the ERA model (wet_ERA) is larger than a given threshold (blue points in Fig. 4).
5) Statistical parameters, including median filters, based on the differences between wet_MWR and wet_ERA, not only at the same measurements but also at neighbouring points. This criterion is used both to detect ice contaminated points and spurious measurements due to for example instrument malfunction (pink points in Fig. 4).
6) Wet_MWR is outside limits (≥0.050 m or < −0.600 m), shown as pink points in Fig. 4.

These criteria need to be tuned to each mission and dataset version, since the data flags and the handling of land, ice or rain contamination varies from one dataset to the next. In addition to the estimation parameters adopted in the objective analysis implementation, these criteria are of crucial importance. An invalid MWR value that has not been flagged will corrupt the estimates of its neighbouring points; on the other hand, each valid MWR value that has been incorrectly flagged as invalid will be replaced by an estimate which is a combined value of other valid MWR and GNSS values and, in cases where the number of observations is zero, by the model value. In any case, the estimated WTC is likely to be less accurate than the original MWR WTC.

Fig. 4 illustrates, for Envisat cycle 62 (top panel) and TOPEX/Poseidon cycle 443 (bottom panel), the points for which the flag_MWR_rej is not zero, that is, the points where new values of the wet tropospheric correction are to be estimated. In addition to ocean points, to help on interpolation to higher data rates, the first land point of each track is also selected, provided it is within 50 km from the coastline (brown points in Fig. 4). This figure demonstrates that the GPD is not merely a coastal algorithm, it is an ocean algorithm, including open-ocean, high latitudes and coastal zones.

In the present implementation rain contamination has not been handled. This is due to the fact that it is not possible to establish robust statistical criteria, solely based on WTC values, to discriminate between rain-contaminated values and strong and rapid variations in the WTC which often occur at low and mid-latitudes. This can only be achieved by means of robust altimeter rain flags, which will be the subject of future work.

In summary, an MWR measurement is considered valid whenever none of the above conditions occur, that is, when flag_MWR_rej is 0. In this case the GPD correction equals the baseline MWR value. In all other cases the point is considered to have an invalid MWR correction and being thus a point for which the correction is to be estimated by the GPD algorithm. Since some rain contaminated values will persist, all valid MWR measurements with values less than −0.6 m are attributed the value −0.6 m and the user may choose to use or discard them.

Fig. 5 shows the percentage of points with flag_MWR_rej ≠ 0, i.e., the number of points to be estimated, relative to the total number

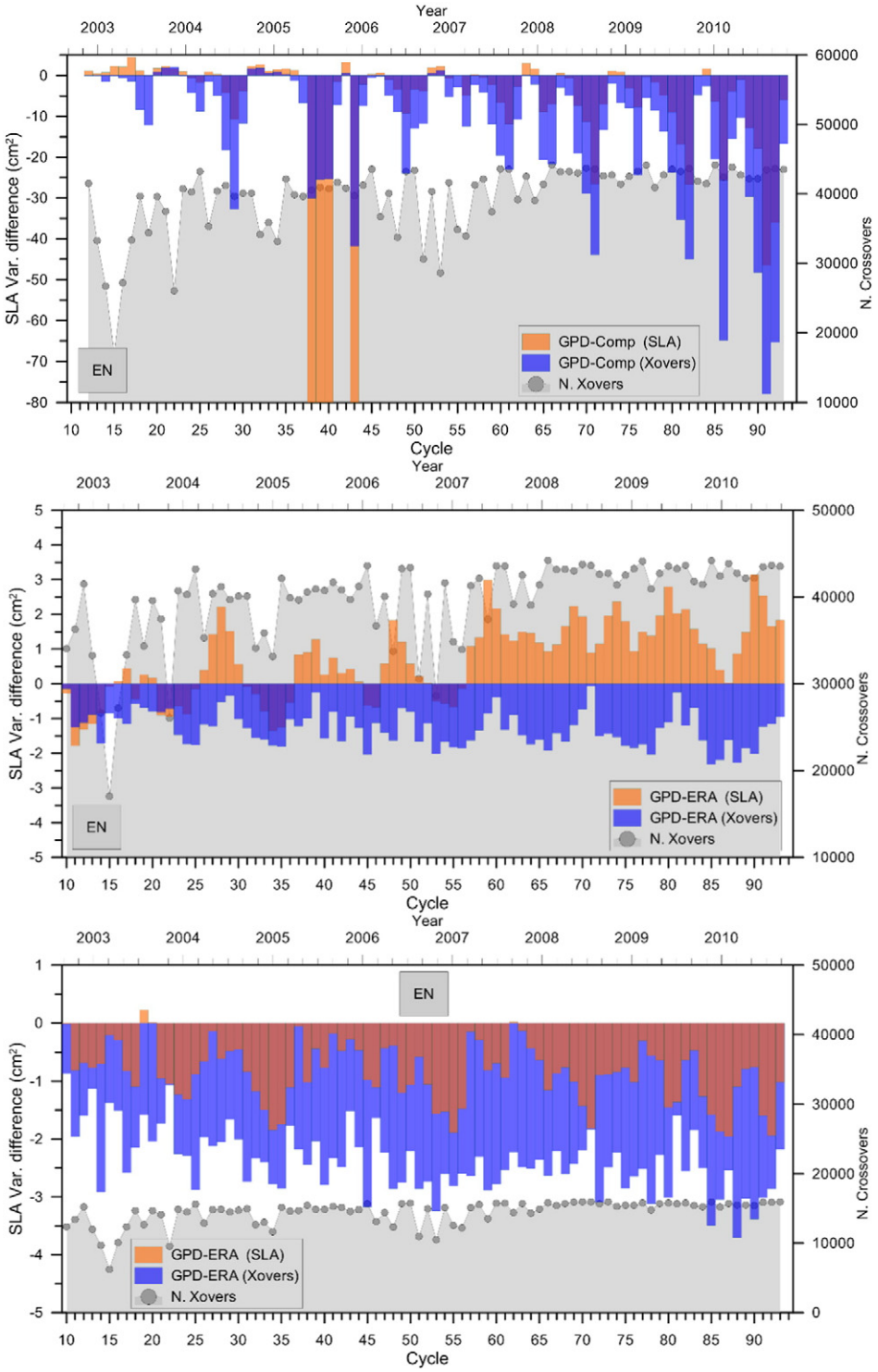

Fig. 15. Temporal evolution of weighted SLA variance differences along track (orange) and at crossovers (blue) between GPD and Comp (top) and ERA (middle) over the period of EN cycles 10 to 93 (2002.4–2010.8). Bottom panel: variance differences between GPD and ERA for points in the latitude band $|\varphi| < 55°$. "N. Crossovers" represents the number of crossovers per cycle.

of points on each cycle of the various missions. Here only points with valid sea level anomaly, used in the validation tasks presented in Section 4, have been used — the corresponding percentages when using all points are larger. It can be observed that, as expected, the number of points to be estimated has a seasonal variation. The mission with the largest percentage of invalid MWR points is Envisat (20%–30%), followed by TOPEX/Poseidon (2%–10%), ERS-1/2 (3%–6%) and Jason-1/2 (1%–3%).

3. The GPD wet tropospheric correction for the six main altimetric missions

In this section we describe the main peculiarities of the implementation of the GPD algorithm to each of the six missions. The main features of the results for all missions are presented.

Since the goal of the GPD methodology is to obtain a global, continuous WTC, by improving the on-board MWR baseline WTC from

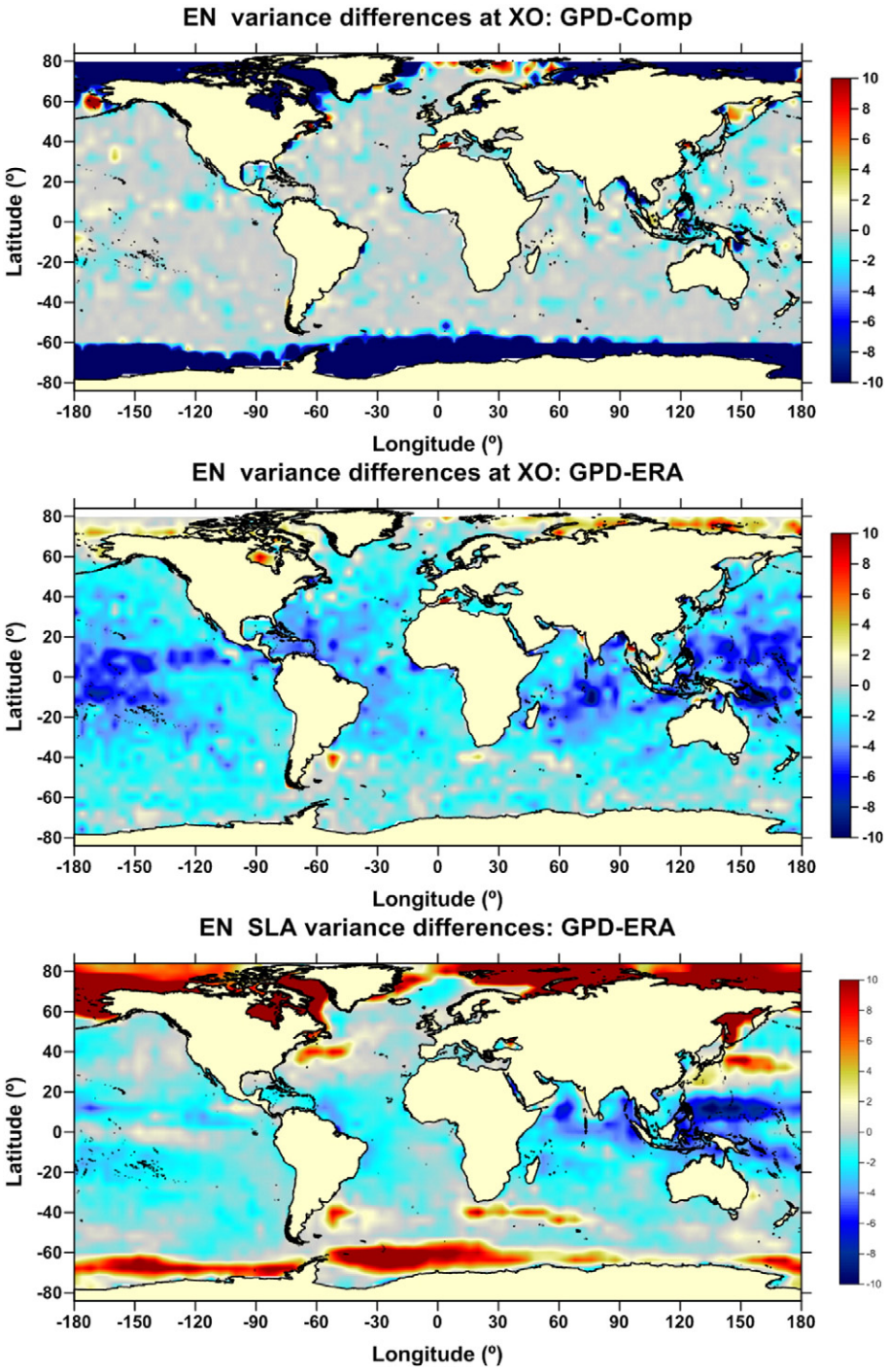

Fig. 16. SLA variance differences at crossovers between GPD and Comp (top) and ERA (middle) over the period EN cycles 10 to 93 (2002.4–2010.8). Bottom panel: corresponding along-track SLA variance differences between GPD and ERA.

erroneous measurements from multiple sources, it is important to characterise each of these errors in the various altimeter products.

Ice, land and rain contamination on the retrieved WTC depends both on the instrument and the retrieval method. For these reasons, these effects are significantly different on the products of the ESA and the reference missions. As mentioned above, the first are 2-band while the second are 3-band radiometers.

The algorithms adopted to retrieve the WTC from the measured brightness temperatures (TB) use statistical methods with coefficients estimated from synthetic databases built using radiative transfer simulations on atmospheric profiles, from radiosoundings or from atmospheric models.

The ERS1–2/MWR algorithm uses a direct log-linear combination of the TBs from the 2 channels and the altimeter-derived wind speed (Eymard, Tabary, Gérard, Le Cornec, & Boukabara, 1986). For Envisat, the retrieval is preformed by a neural network algorithm with the 2 channel TBs and the altimeter backscatter coefficient in Ku band used as inputs (Obligis et al., 2005).

The algorithm for the TMR/JMR/AMR performs the retrieval in three steps: first a term analogous to a surface "radiometer wind" and a term due to cloud liquid water are estimated using a linear combination of the TBs from the 3 channels; then a first approximation of the wet path delay is calculated; finally the wet path delay is obtained by adding to the cloud liquid water term a term obtained from a loglinear

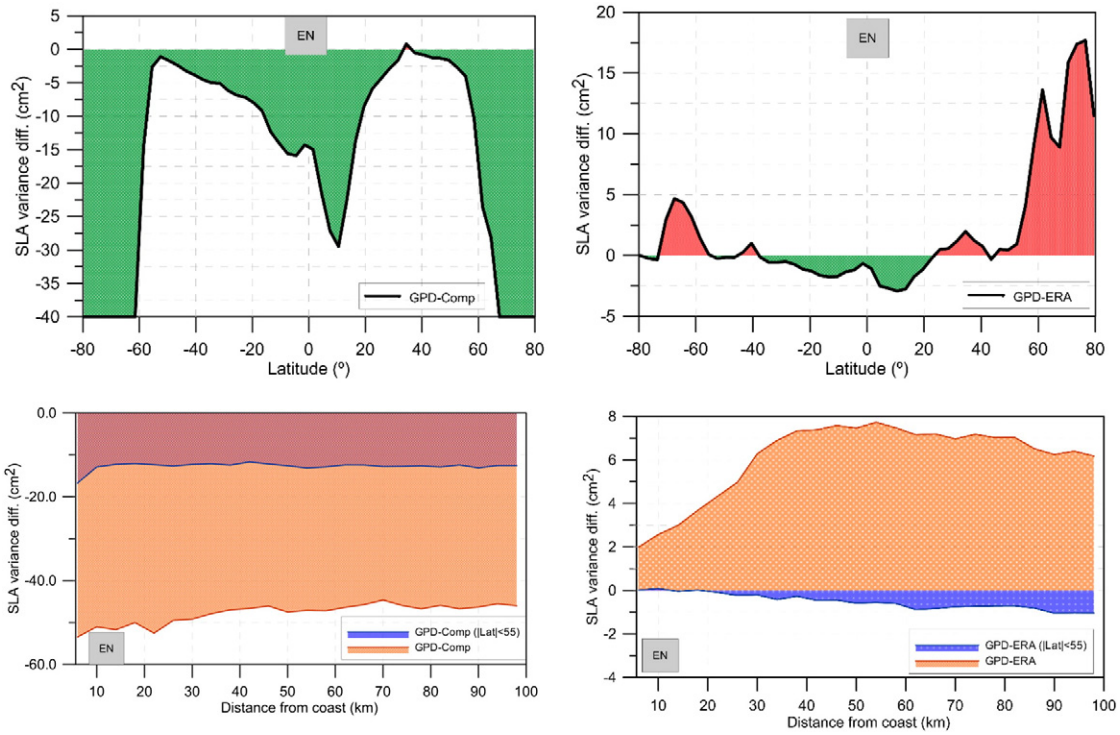

Fig. 17. Variance differences of SLA versus latitude (top) and distance from coast (bottom) between GPD and Comp (left) and ERA (right) for EN cycles 12 to 93 (2002.4–2010.8). In the bottom panels the orange and blue plots represent the results for the whole range of latitudes and for the latitude band $|\varphi| < 55°$, respectively.

combination of the TBs from the 3 channels, with coefficients depending on the "radiometer wind" and wet path delay class interval obtained in the first two steps (Keihm, Janssen, & Ruf, 1995).

Fig. 6 illustrates representative examples of plots along passes of the six altimetric missions showing the GPD wet tropospheric correction (black) against the base MWR (red), ERA Interim (blue) and Composite (green). The shaded areas represent measurements, likely to be corrupted by land (grey), ice (light blue) or instrumental problems (light pink), for which a new estimated has been obtained.

Due to the different characteristics of the instruments and adopted algorithms, the impacts of land, ice and rain in the various products are significantly different as shown in Fig. 6, being much more pronounced in the ESA than in the NASA/CNES missions.

Ice contamination results in extremely negative WTC values (may reach e.g. −0.5 m) in the products of all ESA missions, well far from the expected values of the WTC at high latitudes, in the range −0.1–0.0 m. The same happens with the land contamination in the coastal regions, with less extreme negative values when compared to the previous. Considering the various ESA missions these effects are more marked in the Envisat products when compared to ERS-1/2 suggesting that this maybe due to the different nature of the algorithms used in the WTC retrieval: parametric method for ERS and neural network algorithm for Envisat. The magnitude of these errors in the ESA missions can reach several decimetres, making the original MWR products unusable in the coastal and polar regions (cf. left panels of Fig. 6 and Section 4.1). Due to the different characteristics of the instruments and retrieval algorithms, these effects are much less noticeable in the reference missions. From the latter, TOPEX/Poseidon still evidences significant effects as illustrated in Fig. 6, top right panel. On the contrary, the most recent Jason-1/2 products, already enhanced products using the mixed pixel algorithm (Brown, 2010), evidence only residual ice and land effects as further illustrated in Section 4.2.

The use of 3 bands, apart from increasing the accuracy of the WTC retrieval, it also facilitates the conception of ice and rain detection flags, the low frequency band being of crucial importance in this context. Consequently, ice and rain flags can easily be set for the reference missions (Browm, Desai, Lu, & Sibthorpe, 2008). For the 2-band radiometers the setting of these flags using simple rules based e.g. on thresholds of the differences between the two TBs or between the MWR-based and a model-based WTC is less efficient.

Rain contamination effects are particularly large in Envisat as shown in Fig. 6, still large on ERS-1/2 and less pronounced on all reference missions. Due to the nature of these errors, it is very difficult to establish robust statistical criteria which enables the distinction between unrealistic rain contaminated values and strong signals in the WTC caused by extreme wet conditions. For this reason, in the analysis presented in this paper, apart from extreme negative values spotted by the statistical criteria described in Section 2.3, rain effects have not been corrected and should be subject of future work.

Other sources of error common in many altimeter products are erroneous values of instrumental origin. These are present in all ERS, Envisat and TOPEX/Poseidon products. In TOPEX, they increased in the second half of the mission, having a significant impact on regional sea level estimation, particularly in the Indian Ocean (cf. Section 4.2). The MWR value of these points, often with large positive values, was set to 0.05 m for plotting purposes (see top right panel of Fig. 6). No significant outliers were found in Jason-1 and Jason-2 products, most probably due to the fact that they have been corrected in the most recent versions of the products (Brown, 2010).

Fig. 6 shows that the baseline MWR product used in the GPD and Comp computations are often not exactly the same, the differences being only significant in some regions and for specific periods. It can be observed that the Comp WTC still evidences uncorrected ice contaminated points in some passes of all ESA missions. Moreover, unrealistic

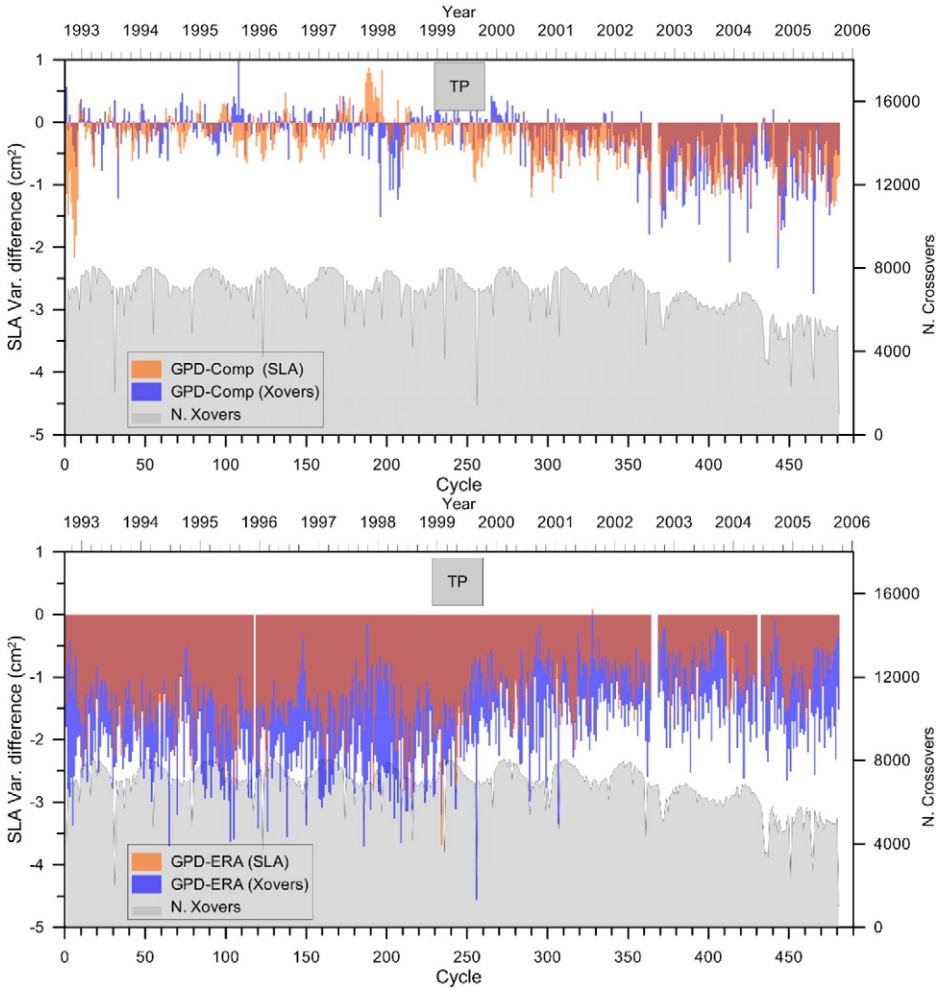

Fig. 18. Temporal evolution of weighted SLA variance differences along track (orange) and at crossovers (blue) between GPD and Comp (top) and ERA (bottom) over the period of TP cycles 1 to 481 (1992.7–2005.8). "N. Crossovers" represents the number of crossovers per cycle.

values can be found in the coastal regions, more evident in TP and only occasionally in ERS, suggesting anomalies in the detrending applied to the ECMWF model values (Mercier et al., 2010). In addition, most anomalous values of instrumental origin are often present in the Comp WTC of all ESA missions and TP.

The GPD corrections have been computed for the whole data set of the aforementioned eight altimetric missions present in RADS (status on January 2015):

- ERS-1 — phases a to g, cycles 1 to 156 (RADS convention) or cycles 1 to 53 (AVISO convention), 1992.8–1996.4;
- ERS-2 — cycles 1 to 169, 1995.4–2011.5,;
- Envisat — cycles 1 to 113, 2002.4–2012.3;
- TOPEX/Poseidon — cycles 1 to 481, 1992.7–2005.8;
- Jason-1 — cycles 1 to 424, 2002.0–2013.5;
- Jason-2 — cycles 1 to 226, 2008.5–2014.7.

Fig. 7 shows the difference between the Composite and GPD corrections, in centimetres. This figure illustrates the magnitude of the differences between the two WTC and the global and continuous coverage of the GPD corrections.

In addition to the WTC value, the algorithm also provides a validation flag (GPD_flag). For all points for which the MWR-based correction has been considered valid, the GPD correction is the same as the baseline MWR WTC and the corresponding GPD_flag is attributed the value 0. For all points with a valid GPD correction estimated from observations, the GPD_flag is set to 1. The points for which no observations exist are attributed the model value and the GPD_flag is set to 2.

Only a very few number of points remain for which the algorithm returns a somehow unexpected value and is properly flagged (GPD_flag = 3). This behaviour seems to be related with locations for which the observations possess very close points with relatively large variations.

For Envisat cycle 62, with 1664091 ocean or coastal points, the algorithm attempted to correct for 24.3% of these points. 6.9% were estimated using valid observations (GPD_flag = 1), 17.4% were set equal to the model value (GPD_ flag = 2, most of these being located at high latitudes) and only 289 (0.02%) have an unexpected estimate (GPD_flag = 3).

Fig. 8 illustrates the GPD formal error for Envisat cycle 62. To understand this figure, we recall that the GPD formal error is a function of the spatial and temporal distribution of the observations relative to the point of computation and also on the signal variance on the same point. The points for which there are no observations and the estimated value equals the model values adopted as first guess, were attributed a formal error of 1.5 cm. It can be observed that these points are mostly located in the polar regions, since in these regions the MWR observations are contaminated by ice.

The great majority of the points have a formal error within 1–2 cm. Considering that each output is a combination of all available observations, in the worst case, the estimation equals the first guess (ERA Interim model value).

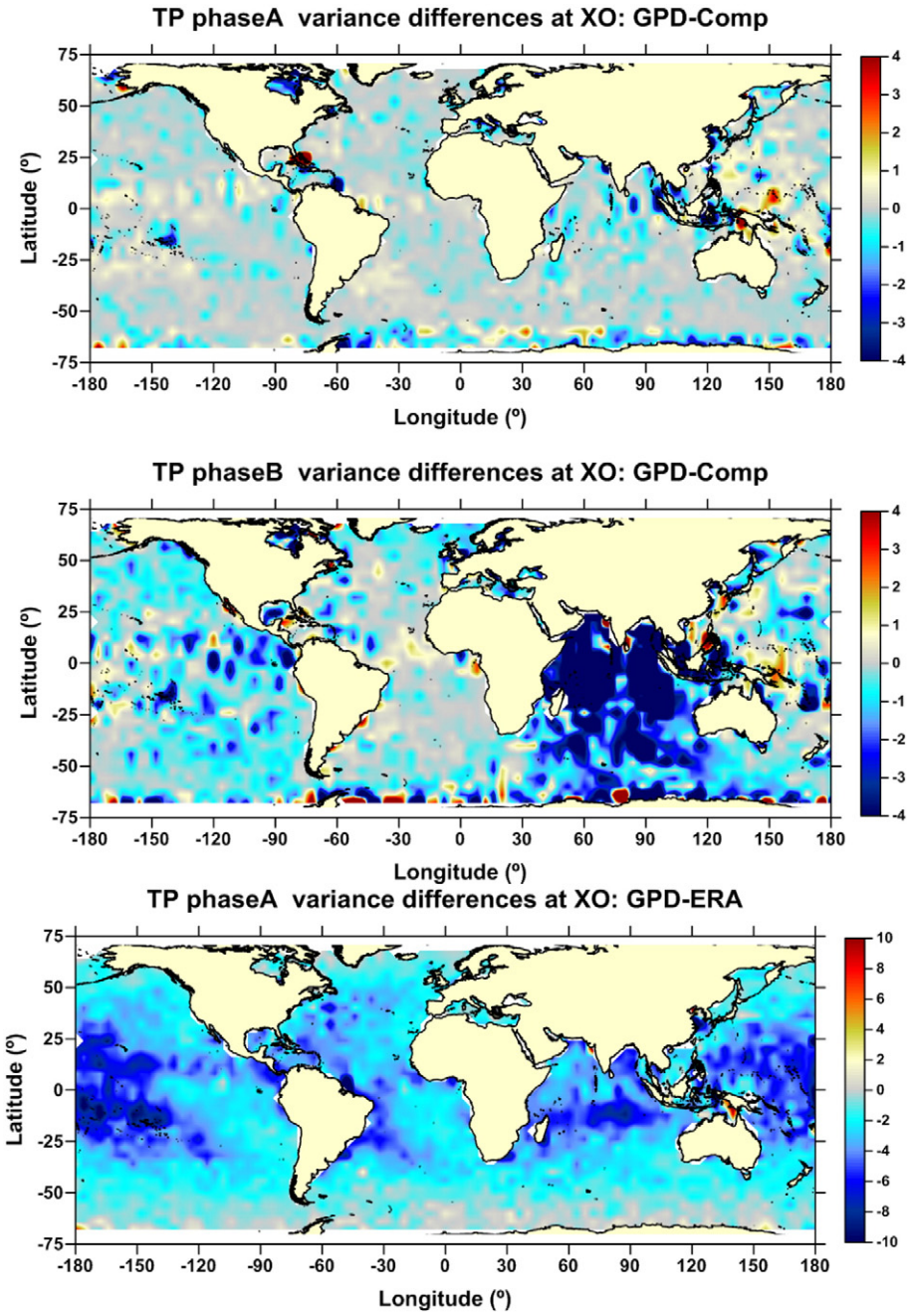

Fig. 19. SLA variance differences at crossovers between GPD and Comp for TP phase A, cycles 1–364, 1992.7–2002.6 (top) and phase B, cycles 369–481, 2002.7–2005.8 (middle). Bottom panel: corresponding results for the difference between GPD and ERA for phase A cycles.

Concerning the availability of valid MWR measurements, the worst cases take place when an isolated segment with all points having invalid MWR measurements occurs (usually when the track is parallel to the coastline), where a contaminated segment of several hundreds of kilometres length may occur. Such an example is Envisat pass 160 along the Portuguese coast (Fig. 3). Due to the time difference between consecutive passes (100 min), in practice in the estimation of a given point only valid measurements from the same pass are used.

Comparing the error map with the map of the standard deviation of the WTC field shown in Fig. 1 it can also be observed that the largest errors are also associated to regions of large field variance

Considering the GNSS-derived path delays, various regions can be identified in Fig. 8, e.g. around European and North American coastlines, where relatively dense networks of coastal stations can be found (c.f. Fig. 1). However, there are many regions, particularly in the African coast, without available GNSS stations for distances of several hundreds of kilometres. In these regions the correction is solely based on valid MWR measurements.

These results also highlight the importance of the choice of the atmospheric model, used as first guess and thus adopted in the absence of valid observations within the space and time search radii. Therefore, the selection of the best available model is of most importance.

4. Validation of the GPD wet tropospheric corrections

The validation of the wet tropospheric correction using independent data sets such as radiosoundings is a difficult task, since these data are sparse and often of not good quality. For this study, GNSS data are not independent from the GPD corrections since they have been used in the computations of the latter. For these reasons, the GPD products

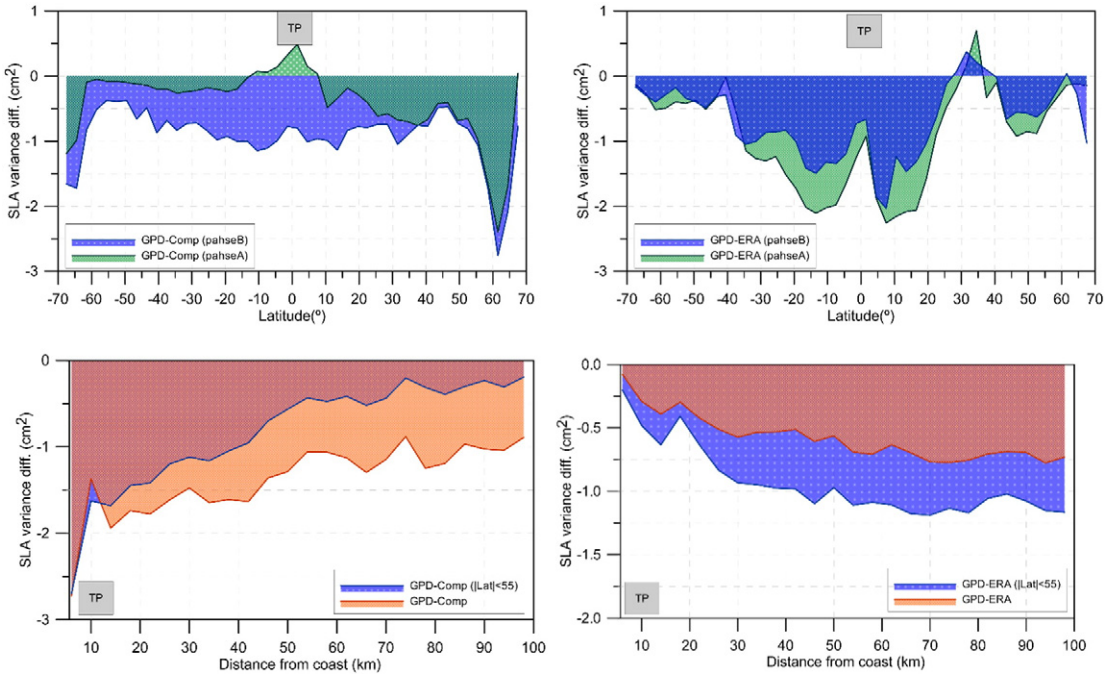

Fig. 20. Top panels: variance differences of SLA versus latitude between GPD and Comp (left) and ERA (right) for TP phase A cycles 1 to 364, 1992.7–2002.6 (green) and phase B cycles 369 to 481, 2002.7–2005.8 (blue). Bottom panels: variance differences of SLA versus distance from coast between GPD and Comp (left) and ERA (right) for TP cycles 1 to 481. In the bottom panels the orange and blue plots represent the results for the whole range of latitudes and for the latitude band $|\varphi| < 55°$ respectively.

have been validated by comparison with the WTC adopted as the reference correction by AVISO, which is the so-called composite correction (Comp) for all missions except J2 and the GDR-D MWR WTC for J2. The Composite Correction is based on the MWR correction, enhanced near the coast (<50 km) and sometimes also at high latitudes by ECMWF model values, somehow adjusted to the last valid MWR point (Mercier et al., 2010). In addition, the GPD corrections are also compared against the WTC from the ERA Interim atmospheric model, the most stable and accurate model at present (Ablain et al., 2015; Legeais et al., 2014). It will be shown that the comparisons with these different corrections allow, not only illustrating the improvements and potential remaining problems in the GPD but also in the other corrections.

A merit of this validation approach is to allow the analysis of the impact of the GPD corrections on sea level studies. For this purpose, various sea level anomaly (SLA) statistical analyses have been performed. The most relevant analyses are presented: weighted variance differences of along-track SLA data and at crossovers for each cycle, SLA variance differences at crossovers mapped globally, SLA variance difference function of distance from the coast and function of latitude. In the first case, the difference between the weighted SLA variances of all along-track points of a given cycle (weights are function of the co-sine of latitude), or of all crossover differences, derived using two different WTC, is estimated. In the second case, crossovers are first estimated from two SLA datasets derived using two different WTC, then the variances of the SLA differences at crossovers are computed in regular latitude × longitude grids (4° × 4°) and subtracted. The last analyses consist in grouping the variance of co-located along-track SLA measurements for a given period, in intervals (or bins) of latitude or distance from coast.

The results are presented in two parts: first the results for the ESA missions are shown, followed by those for the reference altimetric satellites.

4.1. ESA missions

Figs. 9 to 17 illustrate the results for ERS-1, ERS-2 and Envisat. For each satellite various types of analyses were performed, illustrated in three sets of figures:

1) Temporal evolution of sea level anomalies (SLA) weighted variance differences along track and at crossovers between GPD and each of the two corrections, Comp or ERA, over the period of analysis of each mission. To facilitate the analysis, both cycle number and time (year) are used in the x-axis of these figures. Only crossovers with time difference less than 10 days were used. Although the variance reduction at crossover analysis is generally considered a better indicator of the improvement in the various terms used in the SLA computation, including the WTC, it will be shown that the along-track SLA variance is also a useful and complementary diagnostic. It is worth noting that the variance crossover analyses allow the evaluation of SSH error for scales lower than 10 days (comparing SSH consistency between ascending and descending passes), whereas the SLA variance analyses integrates all the temporal scales (the reference being the MSS). Therefore, both approaches are complementary.
2) Geographical pattern of SLA variance differences at crossovers between GPD and each of the two corrections, Comp or ERA over the period of analysis of each mission.
3) Variance differences of SLA versus latitude and distance from coast between GPD and each of the two corrections, Comp or ERA over the period of analysis of each mission. In the analyses function of the distance from coast, two cases are considered: 1) all globe and 2) the latitude band $|\varphi| < 55°$.

In all figures presented in Section 4, whenever the differences were extremely large and exceeded the maximum/minimum values of the y-

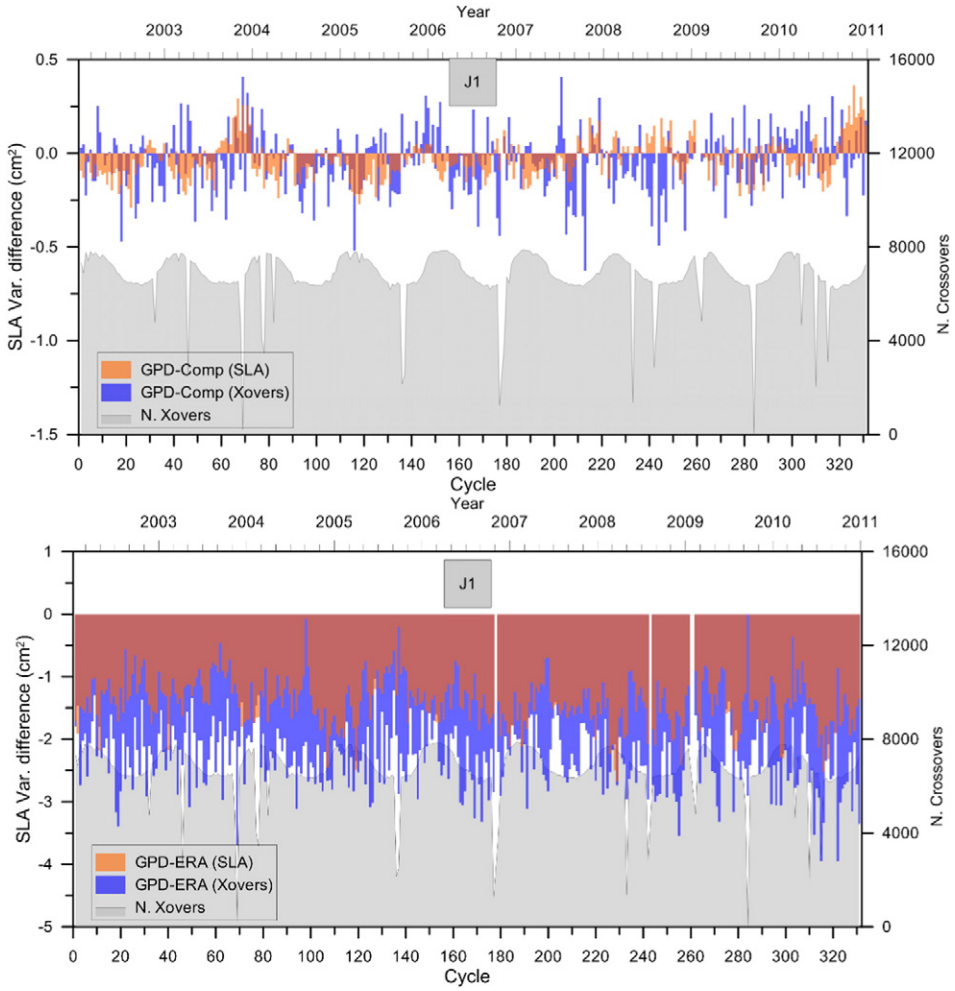

Fig. 21. Temporal evolution of weighted SLA variance differences along track (orange) and at crossovers (blue) between GPD and Comp (top) and ERA (bottom) over the period of J1 cycles 1 to 331 (2002.0–2011.0). "N. Crossovers" represents the number of crossovers per cycle.

axis, for plotting purposes those maximum/minimum values were assumed.

Although the computations have been performed for each mission entire dataset, only the results for the periods for which the composite correction was available, which cover most of each mission lifetime, are presented in this section: ERS-1 — phases c, e, f and g, cycles 89 to 156 (RADS convention) or cycles 15 to 53 (AVISO convention); ERS-2 — cycles 1 to 86, Envisat — cycles 12 to 93.

Figs. 9 to 11 illustrate the results obtained for ERS-1. Fig. 9 shows that the GPD significantly reduces the SLA variance both at crossovers and along-track with respect to the Comp and ERA in a nearly consistent way for all cycles, by 1–4 cm^2.

Fig. 10 illustrates the geographical pattern of the SLA variance differences at crossovers. It can be observed that GPD reduces the variance with respect to the composite correction virtually everywhere and in particular in the coastal and polar regions where the reduction can exceed 10 cm^2. The small number of red spots is most probably related with contaminated MWR measurements which were not properly identified as invalid values.

The comparison with ERA (Fig. 10, bottom panel) shows a pronounced variance reduction mostly in the tropics and equatorial regions, a common feature of the SLA variance differences between MWR-based and model-based ones. A few points, at high latitude and at latitudes close to $\pm 40°$, show small increase in variance and are believed to be related to uncorrected ice contamination and highly energetic current systems, respectively. Most of these features are common to all missions.

These results are further reinforced by those presented in Fig. 11, which represents the SLA variance differences function of latitude and distance from the coast. The most evident feature of the latitude plots is the strong SLA variance reduction of the GPD with respect to Comp at the extreme high latitudes. This is due to the fact that, for ERS-1, the Comp WTC does not correct for most ice contamination (cf Fig. 6).

Again, in Fig. 11, bottom panel, the most striking feature is the significant variance reduction of GPD with respect to Comp in the coastal regions, even when only the band $|\varphi| < 55°$ is considered (cf Fig. 6). The right bottom panel of Fig. 11 reveals that the GPD induces a small SLA variance reduction in the coastal regions with respect to the model-based correction, with decreasing performance for the shortest distances. This feature is common to all ESA missions.

Figs. 12 to 14 illustrate the results for ERS-2, which, in essence, are very similar to those obtained for ERS-1. Comparing to ERS-1, the SLA variance reduction with respect to Comp is larger both at high latitudes and near the coast, indicating that the land and ice contamination in the Comp correction of the ERS-2 products is more pronounced (c.f. Fig. 6). The time evolution of the SLA variance reduction at crossovers and along-track (Fig. 12) shows an even more consistent variance reduction for all cycles, with values from 2 to 6 cm^2.

Figs. 15 to 17 show the results for Envisat. It should be recalled that the Envisat MWR data analysed in this study are the most recent

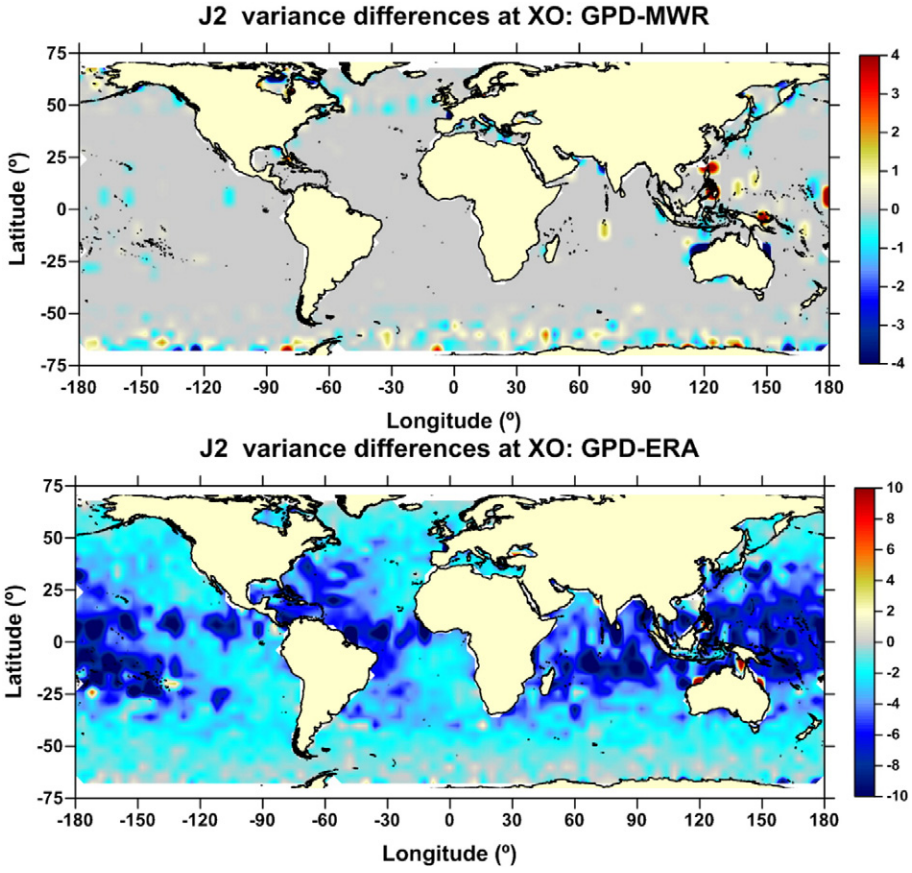

Fig. 22. SLA variance differences at crossovers between GPD and Comp (top) and ERA (bottom) over the period J1 cycles 1 to 259 (2002.0–2009.1).

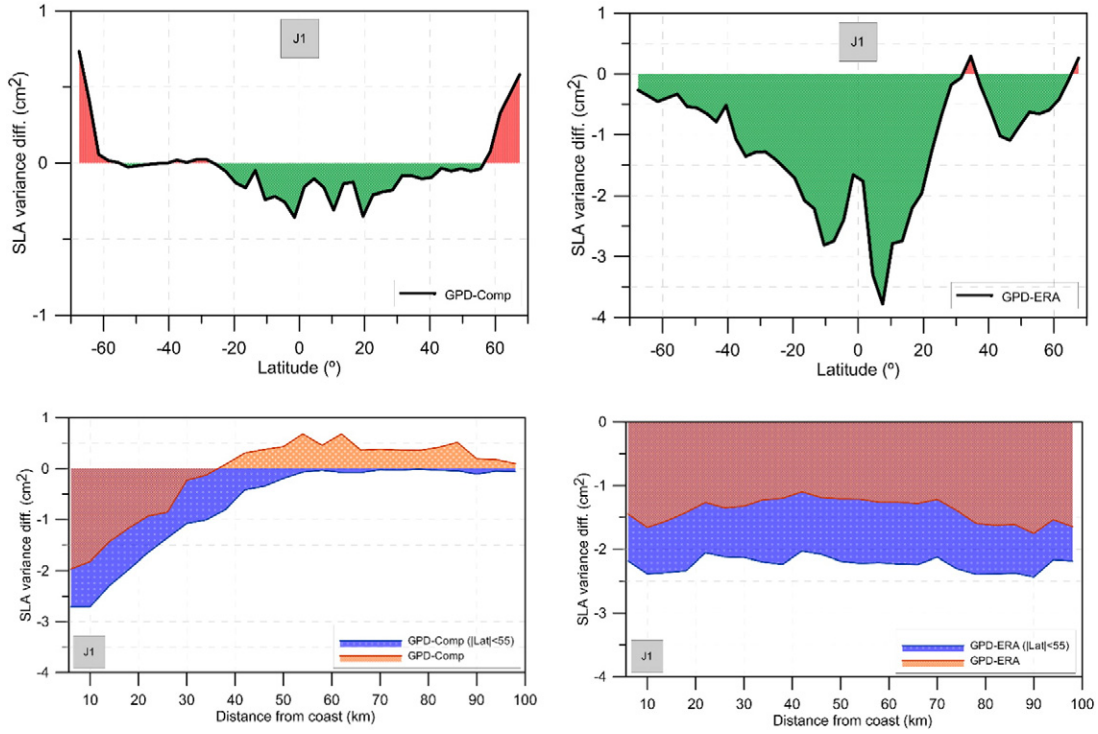

Fig. 23. Variance differences of SLA versus latitude (top) and distance from coast (bottom) between GPD and Comp (left) and ERA (right) for J1 cycles 1 to 331 (2002.0–2011.0). In the bottom panels the orange and blue plots represent the results for the whole range of latitudes and for the latitude band $|\varphi| < 55°$ respectively.

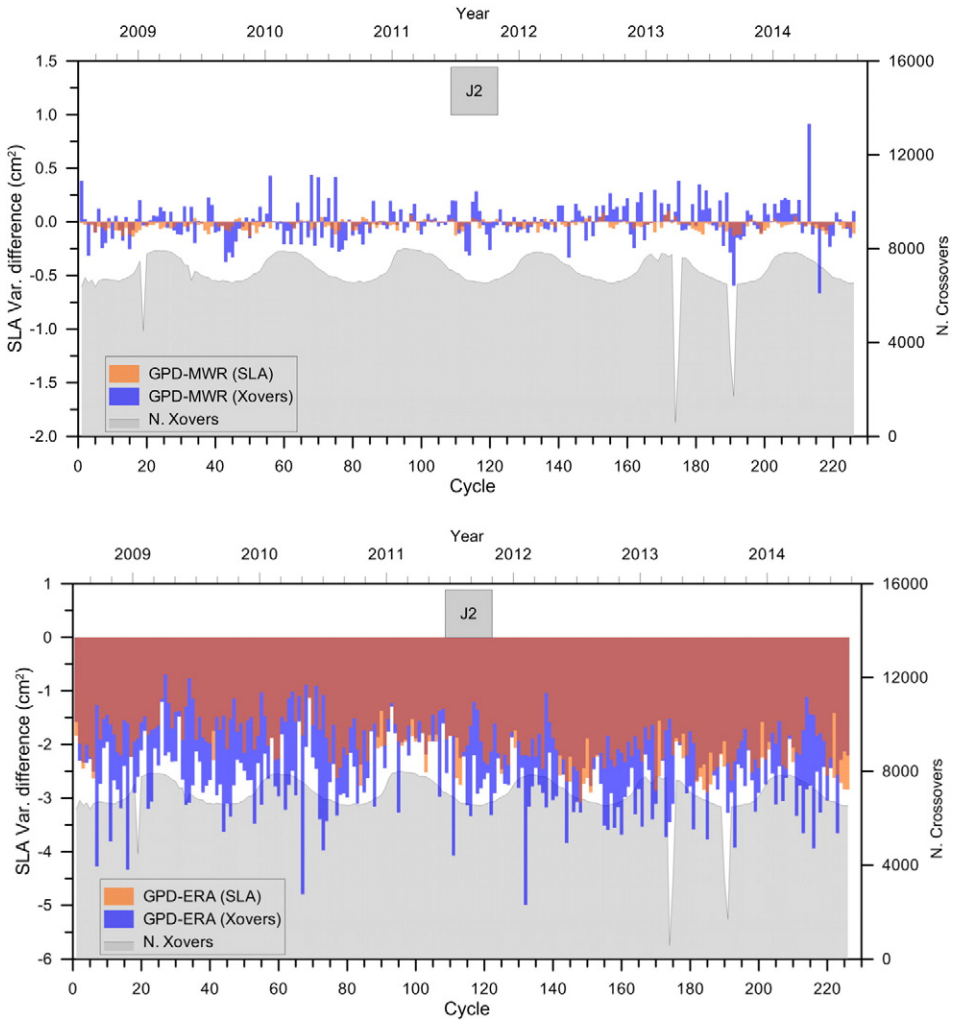

Fig. 24. Temporal evolution of weighted SLA variance differences along track (orange) and at crossovers (blue) between GPD and MWR (top) and ERA (bottom) over the period of J2 cycles 1 to 226 (2008.5–2014.7). For J2 the Comp correction is the baseline MWR WTC. "N. Crossovers" represents the number of crossovers per cycle.

Version V2.1b, provided by CLS, while the Comp correction is based on a previous version of these data.

The top panel of Fig. 15 evidences the strong variance reduction obtained with GPD with respect to Comp. This is explained by the extreme negative values of the Comp correction both at high latitudes and in the coastal regions due to ice and land contamination respectively and also due to the fact that the two corrections are based on different versions of the baseline MWR WTC. The middle panel of Fig. 15 shows a surprising increase in the along-track SLA variance of the GPD with respect to ERA, when considering the whole latitude range, with increasing magnitude with time. However, when selecting only the latitude band $|\varphi| < 55°$, this feature disappears and the GPD correction, as expected from a MWR-based correction, decreases the SLA variance with respect to the model. Note that this behaviour is much less noticeable in the SLA crossover variances.

Fig. 16 further illustrates the uncommon behaviour of the Envisat GPD correction when compared to the model correction. It can be observed that the increase in SLA variance is concentrated at high latitudes, is very strong in the along-track SLA variance map (bottom panel) and much weaker in the crossover variance map (middle panel). The first candidate explanation for these signals is remaining ice contamination in the GPD correction. However, a careful analysis of the Envisat profiles discards this explanation (c.f. Fig. 6). Moreover, ice contamination would also increase the variance at crossovers. When analysing in detail the Envisat along-track profiles, it can be observed that there seems to be an apparent bias (or scale factor) in the Envisat MWR correction at these latitudes, being the MWR values systematically less negative by about 1–1.5 cm over the ERA Interim model values (see Fig. 6). This systematic behaviour explains why these signals are not shown in the crossover analyses since the biases, being approximately the same at the ascending and descending tracks of a given crossover, cancel out. On the contrary, the strong increase in the along-track SLA variance suggests that these biases increase the error in the SLA of these regions. Further research is needed to understand and correct for this apparent anomaly in the Envisat MWR data. In spite of this, the map in the top panel of Fig. 16, showing the crossover variance difference in the SLA between GPD and Comp, proves that the most recent version of the Envisat data is slightly better than the previous one. The strong signals at high latitudes are due to the ice contamination still present in the Envisat Comp correction. Fig. 17 further illustrates the above mentioned features. The top panel of this figure reinforces that, at high latitudes, GPD strongly decreases the SLA variance with respect to Comp while it increases with respect to ERA, with stronger signals in the Northern hemisphere. The bottom panel of Fig. 17 shows the strong improvement of the GPD with respect to Comp in the coastal regions, of the order of 50 cm^2 when considering the whole globe and about 12 cm^2 when the contribution from the high latitudes is removed. The bottom right panel of the same figure shows

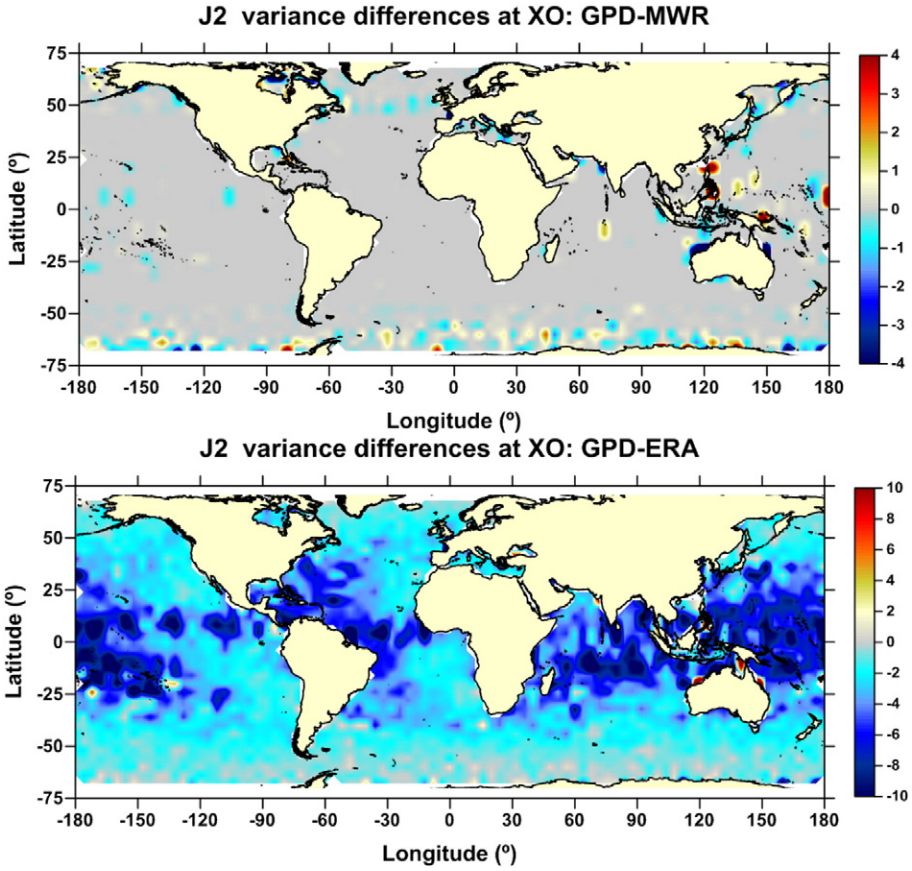

Fig. 25. SLA variance differences at crossovers between GPD and MWR (top) and ERA (bottom) over the period J2 cycles 1 to 226 (2008.5–2014.7).

again the global increase in variance of GPD with respect to the model-derived SLA (7 cm^2), of the same order of magnitude for all distances, which disappears when only the latitude band $|\varphi| < 55°$ is considered, now GPD leading to small SLA variance reduction with respect to ERA.

4.2. Reference missions

Figs. 18 to 26 illustrate the results for TOPEX/Poseidon, Jason-1 and Jason-2. For each satellite the same analyses were performed as for the ESA missions and illustrated in the same way by grouping the results in three sets of figures.

Again, although the computations have been performed for each mission entire dataset, only the results for the periods for which the composite correction was available, which cover most of each mission lifetime, are presented in this section: TP — whole mission, cycles 1 to 481; Jason-1 — cycles 1 to 331, Jason-2 — cycles 1 to 226.

Figs. 18 to 20 illustrate the results obtained for TOPEX/Poseidon. Fig. 18 shows that the results are significantly different before and after about cycle 300. While in the first part of the mission the SLA variance differences with respect to Comp, although globally negative, vary between small positive and negative values of ± 1 cm^2 for the various cycles, in the second part of the mission, both the variance differences at crossovers and along-track become larger and consistently more negative with values up to 2.5 cm^2. The bottom plot of the same figure shows that, in comparison to ERA, the GPD correction is better in the first part of the mission than in the second part. This is likely to be due to anomalies detected in the tape recorder of the TMR, occurred at cycle 370, which caused measurement gaps. The interpolation of these missing measurements originated spurious values that are mostly spotted and corrected by the GPD algorithm (c.f. Fig. 6).

Fig. 19 illustrates the geographical pattern of the variance differences at crossovers. The top and middle panels show the SLA variance differences between GPD and Comp for phase A (cycles 1–364) of the mission, while the middle panel shows the results for phase B (cycles 369–481). It can be observed that the maps of the SLA variance differences between the GPD and Comp are significantly different for the first and second phases of the mission, in agreement with the previous results. In the first phase of the mission the impact of the GPD in the SLA variance is small, of the order of 1 cm^2, except for the coastal regions where the variance reduction is significantly larger. On the contrary, in the second phase of the mission, there are several regions with a variance reduction larger than 4 cm^2, in particular in the Indian Ocean. These large differences are associated to the correction of the aforementioned interpolation anomalies. The bottom panel of Fig. 20 illustrates the expected SLA variance reduction of the GPD correction with respect to the ERA model correction.

The top panel of Fig. 20 shows the SLA variance difference between GPD and Comp (left) and ERA (right), for both phases of the TP mission, reinforcing the data degradation in the second part of the mission. The bottom panel demonstrates the significant improvement of the GPD with respect to Comp (2 cm^2) in the coastal regions, even when only the latitude band $|\varphi| < 55°$ is considered. The bottom right panel shows that, as for ERS-1 and ERS-2, the GPD decreases the SLA variance with respect to the ERA model, with decreasing performance for distances less than 30 km.

Figs. 21 to 23 illustrate the results for Jason-1. Fig. 21 shows that, the mean cycle SLA variance differences between GPD and Comp are small, although globally negative, while, as expected, the differences between GPD and the ERA model are negative. Fig. 22, top panel, shows that GPD and Comp have similar performances except in the coastal regions where GPD reduces the SLA variance by values of 1–4 cm^2. This result

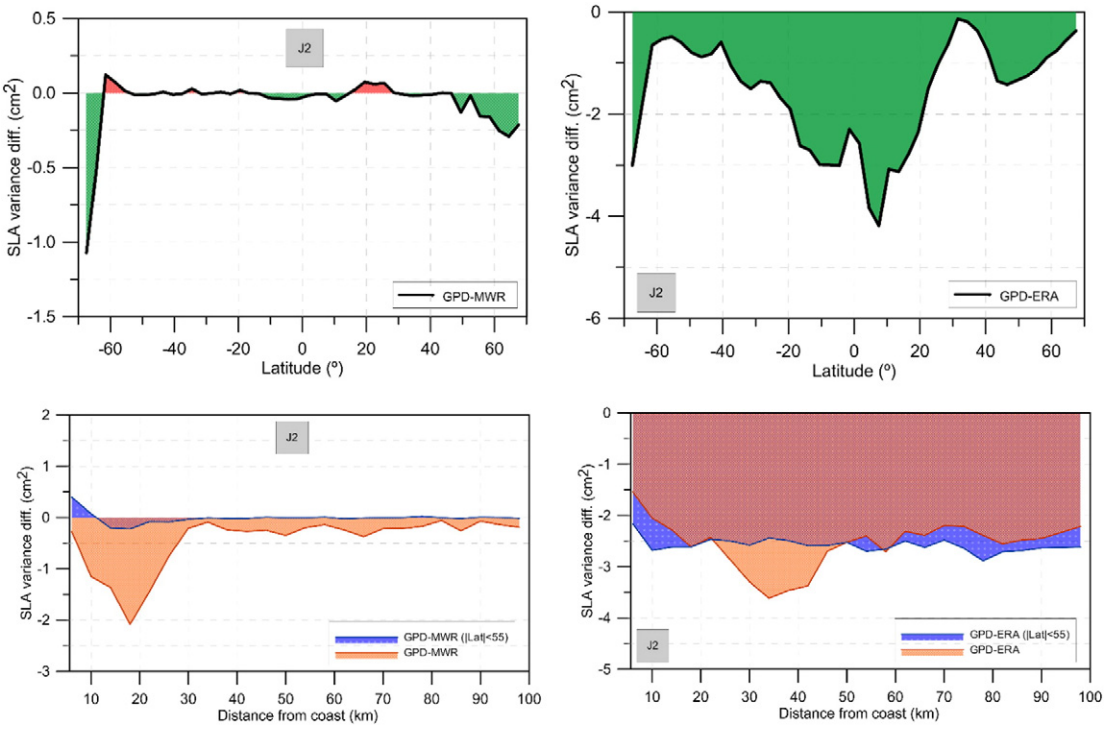

Fig. 26. Variance differences of SLA versus latitude (top) and distance from coast (bottom) between GPD and MWR (left) and ERA (right) for J2 cycles 1 to 226 (2008.5–2014.7). In the bottom panels the orange and blue plots represent the results for the whole range of latitudes and for the latitude band $|\varphi| < 55°$ respectively.

is reinforced by the bottom left plot of Fig. 23. The top left plot of Fig. 23 shows that, at latitudes $|\varphi| > 55°$ the GPD slightly increases the variance with respect to Comp. Note that these differences are very small, less than 1 cm^2, unnoticeable in the plot of the variance difference at crossovers (Fig. 22, top panel). The same can be observed in the bottom left plot of Fig. 23, where small positive values can be observed at distances from coast larger than 40–50 km. It is believed that these features are due to the fact that the base MWR correction used in the GPD and Comp are not exactly the same, suggesting that the version used in Comp is slightly better at the highest latitudes, probably due to a better handling of the ice contamination.

The right plots of Fig. 23 show that the GPD significantly improves the SLA estimation when compared to the ERA model, almost in a uniform way for all distances from the coast, by values up to 2 cm^2, with better performances at the lowest latitudes. This is mostly due to the good performance of the most recent baseline JMR correction present in RADS.

Figs. 24 to 26 illustrate the results for Jason-2. They are very similar to those for Jason-1 with the impacts of the GPD correction being smaller. In comparison to the baseline AMR correction, the GPD causes very small SLA variance differences, only significant in a few coastal regions, mainly at high latitudes, indicating that the GPD corrects for a set of few points with remaining ice contamination in the AMR correction (see Fig. 25, top panel and 26, left panel). When these regions are not considered, GPD shows no significant differences with respect to the GDR-D AMR correction. It should be recalled that while the TMR correction present in RADS is a standard product, the JMR and AMR corrections are already coastal-enhanced products (Brown, 2010). In particular, the GDR-D AMR correction is the result of intensive monitoring and successive calibrations (Brown, 2013).

The right plots of Fig. 26 show very similar results to those obtained for Jason-1 (Fig. 23), i.e., the GPD significantly improves the SLA estimation when compared to the ERA model, in a uniform way for all distances from the coast, by values up to 2 cm^2, with better performances at the lowest latitudes. This is mostly due to the very good performance of the most recent JMR and AMR corrections present in RADS.

5. Conclusions

This paper describes the WTC computed for the set of all ESA and reference missions using the GPD algorithm. Whenever an MWR measurement is considered valid, the correction equals the MWR-based wet path delay. For every ocean point along the altimeter ground track for which the MWR-based WTC has been considered invalid according to a set of predefined criteria, a new estimate is obtained along with its associated error. These include coastal points, but also high latitudes. Therefore, apart from land contamination, ice contamination and outliers are also spotted and corrected. In this way, the algorithm ensures the continuity and consistency of the correction at all latitudes and in the open-ocean/coastal transition zone.

This work shows that for TOPEX/Poseidon, Envisat, ERS-1 and ERS-2 the GPD represents a significant improvement over the AVISO reference composite correction (Comp), particularly in the coastal and polar regions, where significant SLA variance reduction can be observed, both in along-track SLA and at crossovers. The impact is particularly large in all ESA missions due to the strong ice and land contamination present in the baseline MWR products, also partly present in the Comp correction.

For T/P, the most significant result is the strong impact of the correction in the second part of the mission, by correcting for interpolation anomalies present in the TMR products, which affect the SLA variance mainly in the Indian Ocean. If uncorrected, these effects will significantly affect the regional mean sea level trends.

For Jason-1 and Jason-2, for which the MWR correction is already an improved one, the results are different: while for Jason-1 a small improvement is still obtained in the coastal regions, particularly at the

high latitudes, for Jason-2 a smaller but less significant improvement is found.

The comparisons with the ERA Interim model show the expected significant variance reduction in the GPD corrections when compared to the model-based ones, except for Envisat at high latitudes. This result was reinforced by comparison with an independent correction (not shown), based on the combination of data from scanning imaging radiometers (SI-MWR) on board remote sensing earth observation missions and model values, the so-called Data Combination (Dcomb) WTC, Fernandes, Nunes, and Lázaro (2013a), developed in the scope of project CryoSat Plus for Oceans (CP4O), aiming at getting an improved WTC for CryoSat-2, since it does not possess and on-board radiometer. A similar approach to DComb has been used by Stum, Sicard, Carrere, and Lambin (2011) to derive an improved WTC for CryoSat-2.

Additional diagnoses, not shown here, were also performed, for example, the impact of the corrections on the global and regional mean sea level trends (Ablain et al., 2015). Results show that the corrections have a negligible impact on global sea level trend, since no drift corrections were applied to any of the used datasets. In addition, in the computation of the global mean sea level curve, a set of criteria are applied which partly remove the set of points corrected by the GPD algorithm, mainly the points near the coast and at high latitudes. Moreover, in the computation of the mean sea level curve, smoothing is applied to the sea level anomalies, or is implicit when the gridded products are used, which partly corrects for some of the spurious measurements spotted by the GPD methodology.

On the contrary, for most missions, the impact on regional sea level trends was found to be significant, particularly in the coastal and polar regions. In particular, a significant impact was found in the regional mean seal level trends for TOPEX/Poseidon (see SL_cci validation report, http://www.esa-sealevel-cci.org/webfm_send/177), particularly in the Indian Ocean, correlated with the large SLA variance differences shown in Fig. 19, middle panel.

A previous version of the GPD products presented here, with close but slightly worse performances, was adopted as the reference WTC in the generation of the first version of the SL-cci products.

For study of sea level changes, an issue of critical importance is the long-term stability of the corrections. For this purpose, future work will be focused on the identification of possible discontinuities and drifts in the WTC products. In the scope of the SL_cci, the goal is to achieve the GCOS requirement of an uncertainty less than 0.3 mm/year in the mean sea level trend, thus requiring a similar accuracy in the WTC. Although absolute calibration is very difficult to achieve, the inter-comparison of the various datasets (model, MWR and GNSS) and their comparison with other sources such as scanning imaging radiometers will give further insight into these issues. For this purpose, GNSS data for the longest and most stable stations, covering the whole range of wet path delay conditions, processed using state-of-the art and the same methodology, will be used. In addition, recently released and forthcoming atmospheric model reanalyses such as ERA Clim will also be used as possible additional stable sources. A close inspection of the Envisat MWR Version 2.1b correction is required to identify the observed degradation of this correction at high latitudes.

Further research also includes the identification of rain contaminated measurements in all missions.

Finally, in the sequel of the experience acquired with the development of the DComb correction, the next generation of the GPD products shall be based on the DComb methodology, an upgrade of the GPD algorithm, with the SI-MWR data also used as input, the implementation being also extended to CryoSat-2 and SARAL/AltiKa.

Acknowledgements

This work is funded by ESA, in the scope of the Sea Level project of the Climate Change Initiative (CCI), Subcontract No CLS-DOS-14.020 to ESRIN/Contract No. 4000109872/13/I-NB and by FEDER funds (European Union) through the Operational Programme for Competitiveness Factors — COMPETE, and by Portuguese funds through the Fundação para a Ciência e a Tecnologia — FCT, under Project PTDC/MAR/108177/2008.

References

Ablain, M., Cazenave, A., Larnicol, G., Balmaseda, M., Cipollini, P., Faugère, Y., et al. (2015). Improved sea level record over the satellite altimetry era (1993–2010) from the Climate Change Initiative project. *Ocean Science*, *11*, 67–82. http://dx.doi.org/10.5194/os-11-67-2015.

Andersen, O.B., & Cheng, Y.C. (2013). Long term changes of altimeter range and geophysical corrections at altimetry calibration sites. *Advances in Space Research*, *51*(8), 1468–1477. http://dx.doi.org/10.1016/j.asr.2012.11.027.

Andersen, O.B., & Scharroo, R. (2011). Range and geophysical corrections in coastal regions: And implications for mean sea surface determination. In S. Vignudelli, A.G. Kostianoy, P. Cipollini, & J. Benveniste (Eds.), *Coastal altimetry* (pp. 103–145). Berlin/Heidelberg, Germany: Springer-Verlag.

Berg, H. (1948). *Allgemeine Meteorologie: Einführung in die Physik der Atmosphäre*. Bonn, Germany: F. Dümmler.

Bernard, R., Le Cornec, A., Eymard, L., & Tabary, L. (1993). The microwave radiometer aboard ERS1: Part I — Characteristics and performances. *IEEE Transactions on Geoscience and Remote Sensing*, *31*(6), 1186–1198.

Bevis, M., Businger, S., Chiswell, S., Herring, T.A., Anthes, R.A., Rocken, C., et al. (1994). GPS meteorology — Mapping Zenith wet delays onto precipitable water. *Journal of Applied Meteorology*, *33*(3), 379–386. http://dx.doi.org/10.1175/1520-0450.

Boehm, J., Heinkelmann, R., & Schuh, H. (2007). Short note: A global model of pressure and temperature for geodetic applications. *Journal of Geodesy*, *81*, 679–683.

Boehm, J., Niell, A., Tregoning, P., & Schuh, H. (2006). Global Mapping Functions (GMF): A new empirical mapping function based on numerical weather model data. *Geophysical Research Letters*, *33*. http://dx.doi.org/10.1029/2005GL025546 (L07304).

Boehm, J., Werl, B., & Schuh, H. (2006). Troposphere mapping functions for GPS and very long baseline interferometry from European Centre for Medium-Range Weather Forecasts operational analysis data. *Journal of Geophysical Research*, *111*, B02406. http://dx.doi.org/10.1029/2005JB003629.

Bosser, P., Bock, O., Pelon, J., & Thom, C. (2007). An improved mean-gravity model for GPS hydrostatic delay calibration. *IEEE Geoscience and Remote Sensing Letters*, *4*(1), 3–7.

Bretherton, F.P., Davis, R.E., & Fandry, C.B. (1976). A technique for objective analysis and design of oceanographic experiment applied to MODE-73. *Deep-Sea Research*, *23*, 559–582.

Browm, S., Desai, S., Lu, W., & Sibthorpe, A. (November 2008). *Performance assessment of the advanced microwave radiometer after 1 year in orbit, OSTST2008, Nice France, 10–12.*

Brown, S. (2010). A novel near-land radiometer wet path-delay retrieval algorithm: Application to the Jason-2/OSTM advanced microwave radiometer. *IEEE Transactions on Geoscience and Remote Sensing*, *48*, 1986–1992.

Brown, S. (2013). Maintaining the long-term calibration of the Jason-2/OSTM advanced microwave radiometer through intersatellite calibration. *IEEE Transactions on Geoscience and Remote Sensing*, *51*, 1531–1543.

Brown, S., Ruf, C., Keihm, S., & Kitiyakara, A. (2004). Jason microwave radiometer performance and on-orbit calibration. *Marine Geodesy*, *27*, 199–220.

Chelton, D.B., Ries, J.C., Haines, B.J., Fu, L.L., & Callahan, P.S. (2001). Satellite altimetry. In L.L. Fu, & A. Cazenave (Eds.), *Satellite altimetry and earth sciences: A handbook of techniques and applications. Volume 69.* (pp. 1–131). San Diego, CA, USA: Academic.

Cheng, Y.C., Andersen, O.B., & Knudsen, P. (2015). Evaluation of gridded and along-track altimetric data in the Arctic Ocean for climate research. *Marine Geodesy*, *38*(2), 146–162. http://dx.doi.org/10.1080/01490419.2014.954087.

COASTALT (2009). *Wet tropospheric corrections in coastal areas, COASTALT CCN2, deliverable D2.1b v 1.2, 30/06/2009.* (Document code COASTALT-D21b-12).

Dach, R., Brockman, E., & Schaer, S. (2009). GNSS processing at CODE, status report. *Journal of Geodesy*, *83*(3–4), 353–365.

Dach, R., Hugentobler, U., Fridez, P., & Meindl, M. (Eds.). (2007). *Bernese GPS software — version 5.0.* Astronomical Institute, University of Bern.

Davis, J.L., Herring, T.A., Shapiro, I.I., Rogers, A.E.E., & Elgered, G. (1985). Geodesy by radio interferometry: Effects of atmospheric modelling errors on estimates of baseline length. *Radio Science*, *20*(6), 1593–1607.

Dee, D.P., Uppala, S.M., Simmons, A.J., Berrisford, P., Poli, P., Kobayashi, S., et al. (2011). The ERA-Interim reanalysis: Configuration and performance of the data assimilation system. *Quarterly Journal of the Royal Meteorological Society*, *137*, 553–597.

Desportes, C., Obligis, E., & Eymard, L. (2007). On the wet tropospheric correction for altimetry in coastal regions. *IEEE Transactions on Geoscience and Remote Sensing*, *45*, 2139–2149.

Eymard, L., & Obligis, E. (March 13–18, 2006). The altimetric wet tropospheric correction: Progress since the ERS-1 mission. *Proceedings of 15 years of progress in radar altimetry* (Venice, Italy).

Eymard, L., Tabary, L., Gérard, E., Le Cornec, A., & Boukabara, S.A. (1986). The microwave radiometer aboard ERS-1, Part 2: Validation of the geophysical products. *IEEE Transactions on Geoscience and Remote Sensing*, *34*, 291–303.

Fernandes, M.J., Bastos, L., & Antunes, M. (2003). Coastal satellite altimetry — Methods for data recovery and validation. In Tziavos (Ed.), *Proceedings of the 3rd Meeting of the International Gravity & Geoid Commission (GG2002)* (pp. 302–307) (Editions ZITI).

Fernandes, M.J., Lazaro, C., Nunes, A.L., Pires, N., Bastos, L., & Mendes, V.B. (2010). GNSS-derived path delay: An approach to compute the wet tropospheric correction for coastal altimetry. *IEEE Geoscience and Remote Sensing Letters*, *7*, 596–600.

Fernandes, M.J., Lázaro, C., Nunes, A.L., & Scharroo, R. (2014). Atmospheric corrections for altimetry studies over inland water. *Remote Sensing, 6*, 4952–4997.

Fernandes, M.J., Nunes, A.L., & Lázaro, C. (2013). Analysis and inter-calibration of wet path delay datasets to compute the wet tropospheric correction for CryoSat-2 over ocean. *Remote Sensing, 5*, 4977–5005.

Fernandes, M.J., Pires, N., Lázaro, C., & Nunes, A.L. (2013). Tropospheric delays from GNSS for application in coastal altimetry. *Advances in Space Research*, *51*.

Herring, T., King, R., & McClusky, S. (2006). *GAMIT reference manual — GPS analysis at MIT — Release 10.3.* Dep. of Earth, Atm. and Planetary Sciences, MIT.

Hopfield, H.S. (1969). Two-quartic tropospheric refractivity profile for correcting satellite data. *Journal of Geophysical Research*, *74*, 4487–4499.

Keihm, S.J., Janssen, M.A., & Ruf, C.S. (1995). TOPEX/Poseidon microwave radiometer (TMR): III. Wet troposphere range correction algorithm and pre-launch error budget. *IEEE Transactions on Geoscience and Remote Sensing*, *33*(1), 147–161.

Kouba, J. (2008). Implementation and testing of the gridded Vienna Mapping Function 1 (VMF1). *Journal of Geodesy*, *82*, 193–205. http://dx.doi.org/10.1007/s00190-007-0170-0.

Kouba, J. (2009). *A guide to using International GNSS Service (IGS) products.* Geodetic Survey Division, Natural Resources Canada.

Larnicol, G., Cazenave, A., Faugère, Y., Ablain, M., Johannessen, J., Stammer, D., et al. (September 24–29, 2012). ESA sea level climate change initiative. In J. Benveniste, & R. Morrow (Eds.), *Proceedings of the "20 Years of progress in radar altimetry" symposium, Venice, Italy. ESA Special Publication SP-710.*

Leeuwenburgh, O. (2000). Covariance modelling for merging of multi-sensor ocean surface data, methods and applications of inversion. *Lecture Notes in Earth Sciences*, *92*.

Legeais, J.F., Ablain, M., & Thao, S. (2014). Evaluation of wet troposphere path delays from atmospheric reanalyses and radiometers and their impact on the altimeter sea level. *Ocean Science*, *10*, 893–905. http://dx.doi.org/10.5194/osd-11-1613-2014.

Mendes, V.B., Prates, G., Santos, L., & Langley, R.B. (2000). An evaluation of the accuracy of models of the determination of the weighted mean temperature of the atmosphere. *Proceedings of "ION 2000 National Technical Meeting"* (Anaheim, CA).

Mercier, F. (2004). Amélioration de la correction de troposphère humide en zone côtière. *Rapport Gocina, CLS-DOS-NT-04-086.*

Mercier, F., Rosmorduc, V., Carrere, L., et al. (October 4th, 2010). *Coastal and Hydrology Altimetry product (PISTACH) handbook, CLS-DOS-NT-10-246, Issue 1.0.* CNES.

Miller, M., Buizza, R., Haseler, J., Hortal, M., Janssen, P., & Untch, A. (2010). Increased resolution in the ECMWF deterministic and ensemble prediction systems. *ECMWF Newsletter*, *124*, 10–16.

Niell, A.E., Coster, A.J., Solheim, F.S., Mendes, V.B., Toor, P.C., Langley, R.B., et al. (2001). Comparison of measurements of atmospheric wet delay by radiosonde, water vapor radiometer, GPS, and VLBI. *Journal of Atmospheric and Oceanic Technology*, *18*, 830–850.

Obligis, E., Desportes, C., Eymard, L., Fernandes, M.J., Lázaro, C., & Nunes, A.L. (2011). Tropospheric corrections for coastal altimetry. In S. Vignudelli, A.G. Kostianoy, P. Cipollini, & J. Benveniste (Eds.), *Coastal altimetry* (pp. 147–176). Berlin/Heidelberg, Germany: Springer-Verlag.

Obligis, E., Eymard, L., Tran, N., Labroue, S., & Femenias, P. (2005). First three years of the Microwave Radiometer Aboard ENVISAT: In-flight calibration, Processing and Validation of the geophysical products. *Journal of Atmospheric and Oceanic Technology*, *23*(6), 802–814.

Obligis, E., Rahmani, A., Eymard, L., Labroue, S., & Bronner, E. (2010). An improved retrieval algorithm for water vapor retrieval: Application to the Envisat microwave radiometer. *IEEE Transactions on Geoscience and Remote Sensing*, *47*(9), 3057–3064.

Pacione, E., Pace, B., Vedel, H., de Haan, S., Lanotte, R., & Vespe, F. (2011). Combination methods of tropospheric time series. *Advances in Space Research*, *47*, 323–335.

Ruf, C., Keihm, S., & Janssen, M.A. (Jan. 1995). TOPEX/Poseidon microwave radiometer (TMR): I. Instrument description and antenna temperature calibration. *IEEE Transactions on Geoscience and Remote Sensing*, *33*(1), 125–137.

Scharroo, R., Leuliette, E.W., Lillibridge, J.L., Byrne, D., Naeije, M.C., & Mitchum, G.T. (September 20–28, 2012). RADS: Consistent multi-mission products. *Proceedings of symposium on 20 years of progress in radar altimetry* Venice, Italy.

Scharroo, R., Lillibridge, J.L., Smith, W.H.F., & Schrama, E.J.O. (2004). Cross-calibration and long-term monitoring of the microwave radiometers of ERS, TOPEX, GFO, Jason and Envisat. *Marine Geodesy*, *27*, 279–297.

Schüler, J. (2001). *On ground-based GPS tropospheric delay estimation.* (PhD Dissertation) München: Universität der Bundeswehr.

Snajdrova, K., Boehm, J., Willis, P., Haas, R., & Schuh, H. (2006). Multi-technique comparison of tropospheric zenith delays derived during the CONT02 campaign. *Journal of Geodesy*, *79*(10–11), 613–623.

Stum, J., Sicard, P., Carrere, L., & Lambin, J. (2011). Using objective analysis of scanning radiometer measurements to compute the water vapor path delay for Altimetry. *IEEE Transactions on Geoscience and Remote Sensing*, *49*, 3211–3224.

Tournadre, J. (2006). Improved level-3 oceanic rainfall retrieval from dual-frequency spaceborne radar altimeter systems. *Journal of Atmospheric and Oceanic Technology*, *23*, 1131–1149.

Tournadre, J., Lambin-Artru, J., & Steunou, N. (2009). Cloud and rain effects on AltiKa/SARAL Ka-band radar altimeter—Part I: Modeling and mean annual data availability. *IEEE Transactions on Geoscience and Remote Sensing*, *47*, 1806–1817.

Tregoning, P., & Herring, T.A. (2006). Impact of a priori zenith hydrostatic delay errors on GPS estimates of station heights and zenith total delays. *Geophysical Research Letters*, *33*, L23303. http://dx.doi.org/10.1029/2006GL027706.

Verron, J., & Steunou, N. (March 13–18, 2006). ALTIKA: A micro-satellite Ka-band altimetry mission. *Proceedings of 15 years progress in satellite altimetry* (Venice, Italy).

Zumberge, J.F., Heflin, M.B., Jefferson, D.C., Watkins, M.M., & Webb, F.H. (1997). Precise point positioning for the efficient and robust analysis of GPS data from large networks. *Journal of Geophysical Research*, *102*, 5005–5017.